Journal of Medicinal Chemistry

pubs.acs.org/jmc

Article

3CL Protease Inhibitors with an Electrophilic Arylketone Moiety as Anti-SARS-CoV-2 Agents

Sho Konno, Kiyotaka Kobayashi, Miki Senda, Yuta Funai, Yuta Seki, Ikumi Tamai, Laura Schäkel, Kyousuke Sakata, Thanigaimalai Pillaiyar, Akihiro Taguchi, Atsuhiko Taniguchi, Michael Gütschow, Christa E. Müller, Koh Takeuchi, Mikako Hirohama, Atsushi Kawaguchi, Masaki Kojima, Toshiya Senda, Yoshiyuki Shirasaka, Wataru Kamitani, and Yoshio Hayashi*

Cite This: https://doi.org/10.1021/acs.jmedchem.1c00665

Read Online

ACCESS | Metrics & More | Article Recommendations | Supporting Information

ABSTRACT: The novel coronavirus, SARS-CoV-2, has been identified as the causative agent for the current coronavirus disease (COVID-19) pandemic. 3CL protease (3CL^{pro}) plays a pivotal role in the processing of viral polyproteins. We report peptidomimetic compounds with a unique benzothiazolyl ketone as a warhead group, which display potent activity against SARS-CoV-2 3CL^{pro}. The most potent inhibitor YH-53 can strongly block the SARS-CoV-2 replication. X-ray structural analysis revealed that YH-53 establishes multiple hydrogen bond interactions with backbone amino acids and a covalent bond with the active site of 3CL^{pro}. Further results from computational and experimental studies, including an *in vitro* absorption, distribution, metabolism, and excretion profile, *in vivo* pharmacokinetics, and metabolic analysis of YH-53 suggest that it has a high potential as a lead candidate to compete with COVID-19.

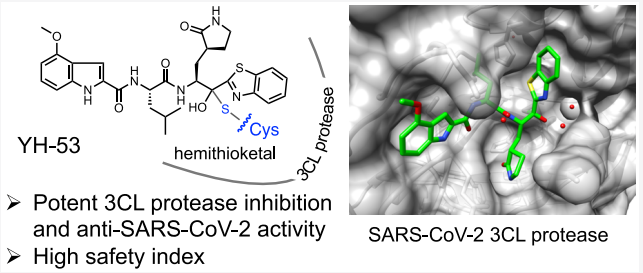

INTRODUCTION

In December 2019, an outbreak of coronavirus disease-19 (COVID-19) emerged in Wuhan, China and evolved into a pandemic with major effects on the public health care system and the global economy. Severe acute respiratory syndrome coronavirus 2 (SARS-CoV-2) has been identified as an etiological agent[1−4] and shares a very high RNA genome (~80%) similarity with that of SARS-CoV-1,[2,5] a virus that caused the SARS outbreak in 2003.[6,7] As of March 5, 2021, more than 110 million cases of COVID-19 and over 2.5 million deaths have been reported. Recently, several vaccines protecting against SARS-CoV-2 were approved in many countries. With respect to the treatment of SARS-CoV-2, however, drug repositioning is a promising approach to discovery of new indications from existing clinical drugs since they can become available within a short development period. Considering the seriousness and the pandemic of SARS-CoV-2 infection, a huge effort has been made to reposition approved drugs that are known to act against related pathogens.[8,9] Remdesivir, an inhibitor of RNA-dependent RNA polymerase (RdRp), which was originally developed for use against ebolavirus,[10] has been approved for the treatment of patients with severe COVID-19 as a directly acting antiviral agent.[11] The approved vaccines and drugs for treatment of COVID-19 give us hope to cope with the pandemic, but the variety of specific inhibitors which fight SARS-CoV-2 infection with a different mechanism of action are urgently needed to reduce the cases and also the severity and fatality rates. Examples include α-ketoamide[12] and aldehyde inhibitors[13] with potent anti-SARS-CoV-2 activity through their protease inhibition. These compounds have good pharmacokinetics and no significant toxicity.

Coronavirus is an enveloped, single-stranded, positive-sense RNA virus that is manipulated directly by a host's translational system. Its replicase gene encodes for two large overlapping polyproteins, pp1a and pp1ab, which are required for viral replication and transcription.[14] The functional proteins are released from these polyproteins by extensive proteolytic processing, predominantly by the 3C-like protease (3CL^{pro}), also referred to as the main protease (M^{pro}), and the papain-like protease (PL^{pro}).[15−19] 3CL^{pro}, a cysteine protease that is active at 11 conserved sites within the large viral polyproteins pp1a and pp1ab, is essential for viral replication and multiplication.[20] The indispensable role of 3CL^{pro} in the viral life cycle and the absence of closely related human homologues establish 3CL^{pro} as an ideal target for the development of antiviral agents for coronavirus diseases.[7,15,21] A large part of the drug discovery program for the

Special Issue: COVID-19

Received: April 12, 2021

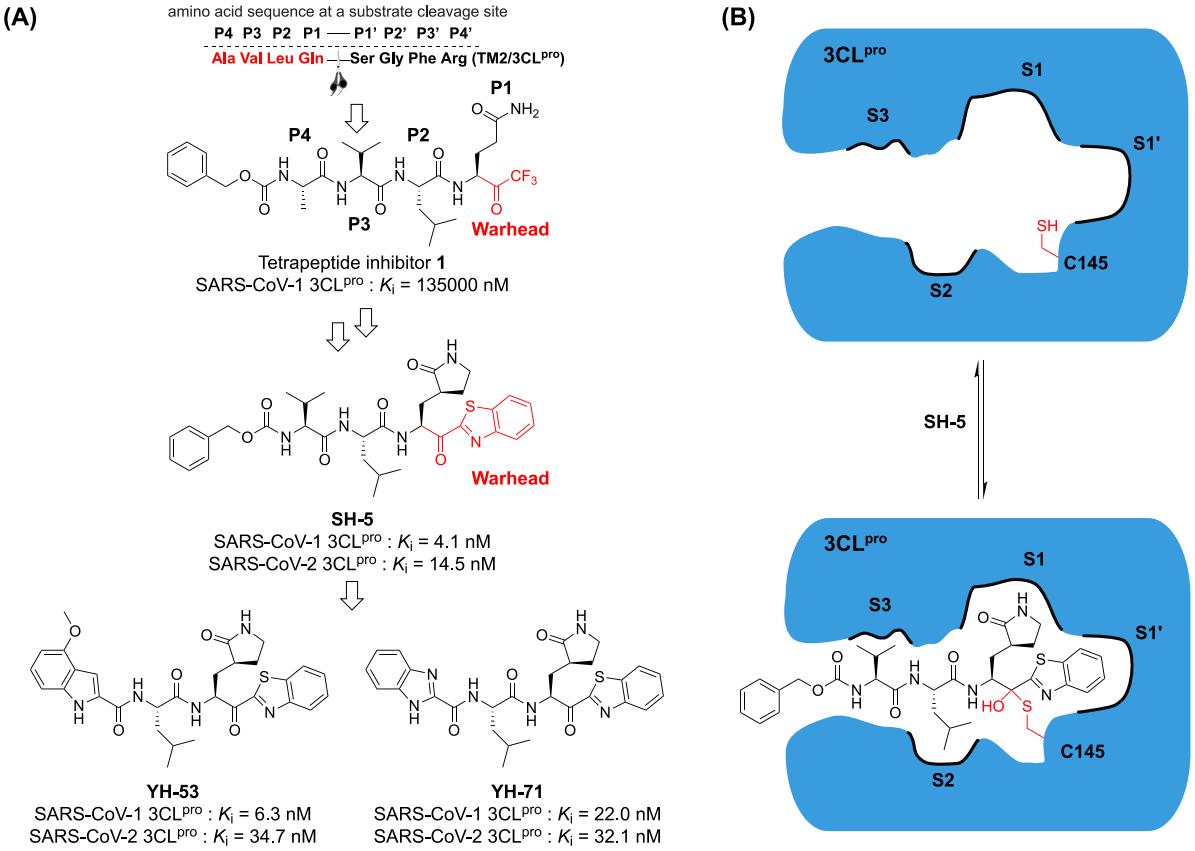

Figure 1. 3CL protease inhibitors for SARS-CoV-1 with electrophilic arylketone warhead. (A) Structures of 3CL^{pro} inhibitors **1**, SH-5, YH-53, and YH-71. SH-5 contains a tripeptide scaffold with a warhead and a carbamoyl unit at P4. YH-53 and YH-71 consist of a dipeptide scaffold with a warhead and a heteroaromatic unit at P3. (B) Proposed mechanism of inhibition by SH-5. Once SH-5 is bound to the enzyme, the active site Cys145 of 3CL^{pro} attacks the ketone of SH-5 to afford a reversible covalent bond. The hemithioketal intermediate would then be stabilized by an oxyanion hole.

control of SARS in 2003 and MERS in 2012 has therefore been dedicated to the development of potent 3CL^{pro} inhibitors.[7,15,21] 3CL^{pro} of SARS-CoV-2 shows 99% homology and 96% identity to that of SARS-CoV-1.[10]

We have been developing a series of substrate-derived inhibitors of SARS-CoV-1 3CL^{pro} since the outbreak of SARS in 2003.[22−27] Inhibitors SH-5, YH-53, and YH-71 (previously designated as **2i**, **5h**, and **5n**, respectively)[25,27] that contain a unique benzothiazolyl ketone as the P1′-directed warhead were developed from a tetrapeptide inhibitor (**1**) by incorporation of a trifluoromethylketone moiety. They are of particular interest because they display potent SARS-CoV-1 3CL^{pro} inhibitory activities with K_i values of 4.1,[25] 6.3[27] and 22[27] nM, respectively (Figure 1A). The electrophilic ketone warhead forms a reversible covalent bond with the nucleophilic thiolate of the active site Cys145 in SARS-CoV-1 3CL^{pro}, resulting in a hemithioketal intermediate that transiently inactivates the enzyme (Figure 1B). The reversibility of this inhibition reduces the chances of the nonspecific irreversible reaction of numerous mammalian thiols and also the risk of clinically undesirable side effects or immune reactions. Given the highly structural identity of 3CL^{pro} between SARS-CoV-1 and SARS-CoV-2, it is expected that these inhibitors would show anti-SARS-CoV-2 activity through 3CL^{pro} inhibition.[10] In the present study, we repositioned and investigated the potential of our SARS-CoV-1 inhibitors as anti-SARS-CoV-2 drugs. In particular, inhibitors containing an indole moiety at the P3-position and the benzothiazolyl ketone as the reactive warhead as in YH-53 showed an extremely potent inhibitory activity against 3CL^{pro} of SARS-CoV-2 and completely blocked viral replication in Vero cells. To understand the binding mode of these inhibitors, cocrystal structures of SARS-CoV-2 3CL^{pro} in complexes with YH-53 and SH-5 were determined, providing useful insights into the precise interaction between the inhibitors' structures and the relevant substrate pockets of the viral protease. Additional comprehensive characterization such as *in vitro* absorption, distribution, metabolism, and excretion (ADME), toxicity, pharmacokinetics, computational principal component analysis, and metabolic analysis have shown YH-53 to be an attractive lead compound in the development of anti-SARS-CoV-2 agents.

RESULTS

Inhibitory Activities for 3CL Protease. The inhibitors SH-5, YH-53 and YH-71 were prepared using our previously published synthetic methods.[25,27] Using our recently developed biochemical assay, we first examined the inhibitory activity of SH-5, YH-53, and YH-71 against SARS-CoV-2 3CL^{pro} (Figure 2A and C). The full length 3CL^{pro} of SARS-CoV-2, His-tagged at the C-terminus, was expressed in *Escherichia coli*.[28] The three inhibitors, SH-5, YH-53, and YH-71 were shown to be potent inhibitors of SARS-CoV-2 3CL^{pro}, with K_i values in the nanomolar range (SH-5: K_i = 14.5 ± 1.7 nM; YH-53: K_i = 34.7 ± 2.1 nM; YH-71: K_i = 32.1 ± 3.3 nM). The inhibition mode of the most potent inhibitor, SH-5, was determined and was shown to be competitive (Figure 2B). This confirms the predicted mechanism of action, a tight and reversible binding, and interaction with the active site in the S4-S1′-pockets. Hattori

https://doi.org/10.1021/acs.jmedchem.1c00665
J. Med. Chem. XXXX, XXX, XXX−XXX

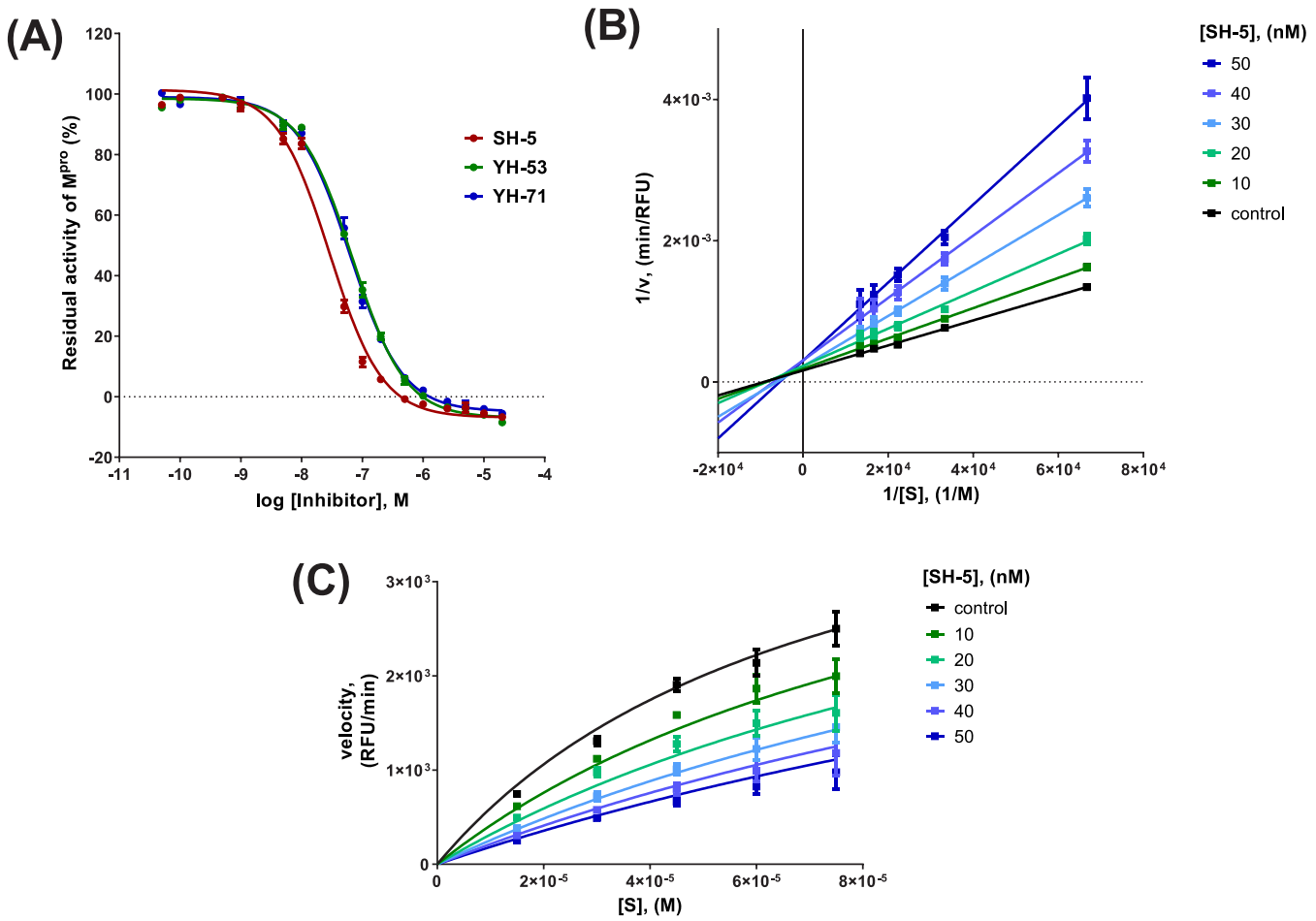

Figure 2. SARS-CoV-2 3CL^{pro} inhibitory assay. (A) Concentration-dependent inhibition of SARS-CoV-2 3CL^{pro} by SH-5, YH-53 and YH-71. Reactions were monitored for 10 min. Data points represent mean values ± SEM from three independent experiments. K_i values were calculated using the Cheng−Prusoff equation and are noted in Figure 1. The K_m value of the substrate was 48.4 μM. (B) Lineweaver−Burk plot for SH-5 inhibition of SARS-CoV-2 3CL^{pro} at 15, 30, 45, 60, and 75 μM of fluorogenic substrate and 0, 10, 20, 30, 40, and 50 nM of the inhibitor SH-5. Three independent experiments were performed, and reactions were monitored for 10 min. The common intercept on the ordinate indicates a competitive inhibition type. (C) Global fit of kinetic data from (B) for competitive enzyme inhibition. The best fit value of K_i 19.8 ± 2.3 nM was in the same range as the value calculated by the Cheng−Prusoff equation (see Figure 1).

et al. recently reported the SARS-CoV-2 3CL^{pro} inhibitory activity of YH-53 with K_i = 17.6 nM, which is consistent with our data.[29] Peptidomimetic benzothiazolyl ketone inhibitors have already been studied as inhibitors of several serine and cysteine proteases and the reversible formation of hemi(thio)ketal adducts has been demonstrated.[30−33] The reversible mode of action is supported by the analysis of the progress curves which did not show time-dependent inhibition (Figure S1). We also carried out an NMR titration experiment study, which confirmed that YH-53 bind to SARS-CoV-2 3CL^{pro} in 1:1 stoichiometry and with slow exchange kinetics, as expected from the tight interaction between YH-53 and the target protein (Figure S2).

X-ray Crystallography of SARS-CoV-2 3CL Protease and Comparison of YH-53 and SH-5. We next determined crystal structures of the 3CL^{pro}-YH-53 and -SH-5 complexes at 1.65 and 2.15 Å resolutions, respectively, to reveal the binding mode of such peptide-type inhibitors (Table S1, Figure 3A and B). The crystal structures showed that both inhibitors have extended conformations which interact with 3CL^{pro} and the main chains of the inhibitors interact with the 12th β-strand of the 3CL^{pro} in an antiparallel manner. Moreover, Cys145 forms a tetrahedral hemithioketal bond with the carbonyl carbon at the P1 position (Figure S3). Since the chemical structures of the P1' (benzothiazole), P1 (pyrrolidin-2-one), and P2 (isobutyl) moieties of the two inhibitors are identical, the C-terminal portion of the inhibitors interacts with the 3CL^{pro} in the same manner (Figure 3C). While the benzothiazole, pyrrolidine-2-one, and isobutyl groups are well accommodated in the S1′, S1, and S2 pockets, respectively (Figure 3D and E), only the pyrrolidin-2-one group is completely buried in the protein. The carbonyl and amine group of pyrrolidine-2-one at P1 position interacts with the side chain of His163 and Glu166, respectively. Interestingly, nitrogen and sulfur atoms of the benzothiazole form a hydrogen bond network with water and His41 in the active site, respectively. Since the chemical structures of the N-terminal part of YH-53 and SH-5 are different, the inhibitors provoke different interactions with the S3 and S4 specificity pockets of the target. In the SH-5 complex, the isopropyl group at the P3 position is exposed to the bulk solvent (Figure 3E). The benzyloxy group at the P4 position interacts with Gln189, Thr190, and Ala191, and its one face is exposed to the solvent. At the P3 and P4 residues, only small conformational changes were observed when the structure was compared with the inhibitor-free form (PDB ID: 6M2Q). On the other hand, YH-53 binding induced a larger conformational change in a loop

https://doi.org/10.1021/acs.jmedchem.1c00665
J. Med. Chem. XXXX, XXX, XXX−XXX

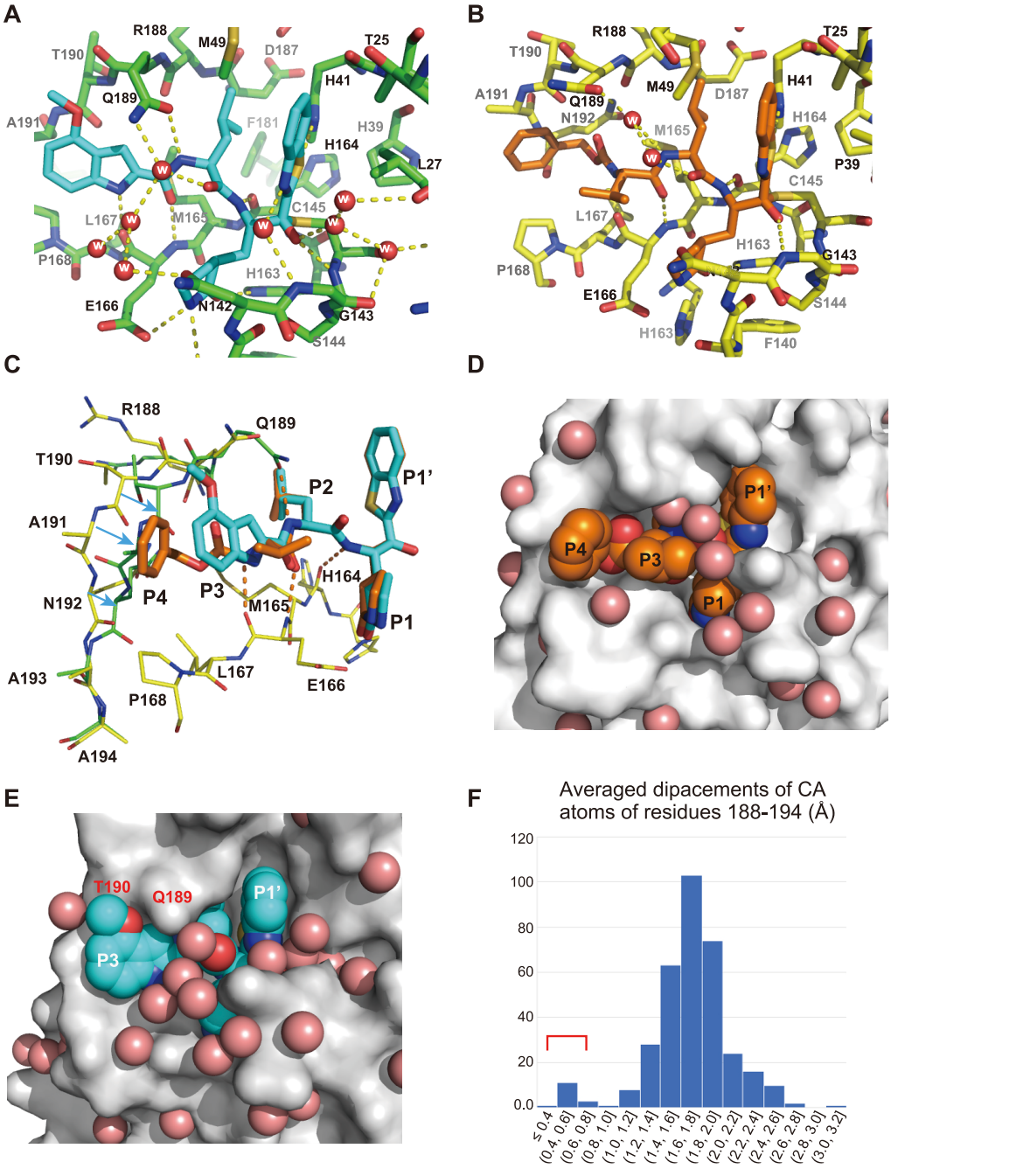

Figure 3. Structures of SARS-CoV-2 3CL^{pro} with its inhibitors. (A, B) Inhibitor binding sites of 3CL^{pro} for YH-53 (A) and SH-5 (B). Protein carbons for YH-53 and SH-5 complexes are shown in green and yellow, respectively. YH-53 (A) and SH-5 (B) are in cyan and orange, respectively. Water molecules are labeled with "w". (C) LSQ superposition of the YH-53 and SH-5 complexes using 281 CA atoms (RMSD = 0.594 Å). Cyan arrows show the shifts of loop residues. Atom color scheme is the same as that in panels (A) and (B). (D, E) Surface representations of SH-5 and YH-53 binding sites. Atom color scheme is the same as that in panels (A) and (B), but water molecules are in salmon pink. (F) Distribution of averaged Cα-atom displacements of residues 188−194 in 3CL^{pro}. We performed least-squares fittings of 3CL^{pro} structures obtained from the PDB onto the present 3CL^{pro}-YH53 structure (PDB ID: 7E18) with residues 10−290 (Cα atoms) using program LSQKAB in the CCP4 program suite,[34] and 345 3CL^{pro} structures with the RMSD values less than 2.0 Å were selected for the following calculation. The averaged Cα-atom displacement of residues 188−194 was calculated for each superposed structure using the LSQKAB output that contains Cα-atom displacements of the superposed residues, and the histogram was prepared. Twelve structures indicated with the red bracket have loop structures similar to the YH-53 complex. The others have loop structures similar to the inhibitor-free form.

region (residues 188−194) of 3CL^{pro}, and the residues of the loop region were shifted toward the inhibitor by approximately 2.5 Å. As a result, Thr190, Gln189, and the backbone Glu166 cover the 4-methoxy-indole group at the P3 position of YH-53, which is important for the enhanced inhibitory activity. The side chain carbonyl of Gln189 forms a hydrogen bond with the main chain amide group at the P2 position. As a result, the active site in the YH-53 complex has a more closed conformation (Figure 3E). Since the methoxy group on the P3 indole group is not involved in strong interactions with the protein, YH-71, an inhibitor with P3-benzimidazole, can be expected to bind 3CL^{pro} similarly to YH-53 with a conformational change of the loop

https://doi.org/10.1021/acs.jmedchem.1c00665
J. Med. Chem. XXXX, XXX, XXX−XXX

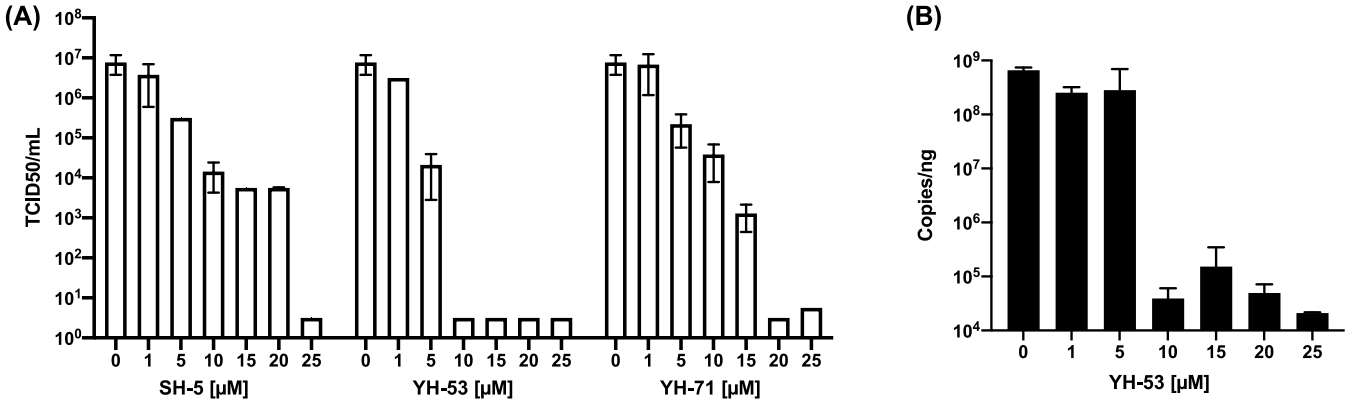

Figure 4. Anti-SARS-CoV-2 activities of SH-5, YH-53 and YH-71 in Vero cells. (A) Antiviral activity of SH-5, YH-53, and YH-71. Vero cells were infected with SARS-CoV-2 using a multiplicity of infection (MOI) of 0.01. The inhibitors SH-5, YH-53, and YH-71 (1−30 μM) were treated to the infected cells then incubated for 48 h at 37 °C. The viral/serum mixtures were transferred to the flesh Vero cell and incubated for 24 h at 37 °C, followed by subject to the plaque assay. Data points represent mean values ± SEM from three independent experiments. (B) Total viral RNA of infected cells treated with YH-53 was analyzed by qPCR. Data points represent mean values ± SEM from three independent experiments.

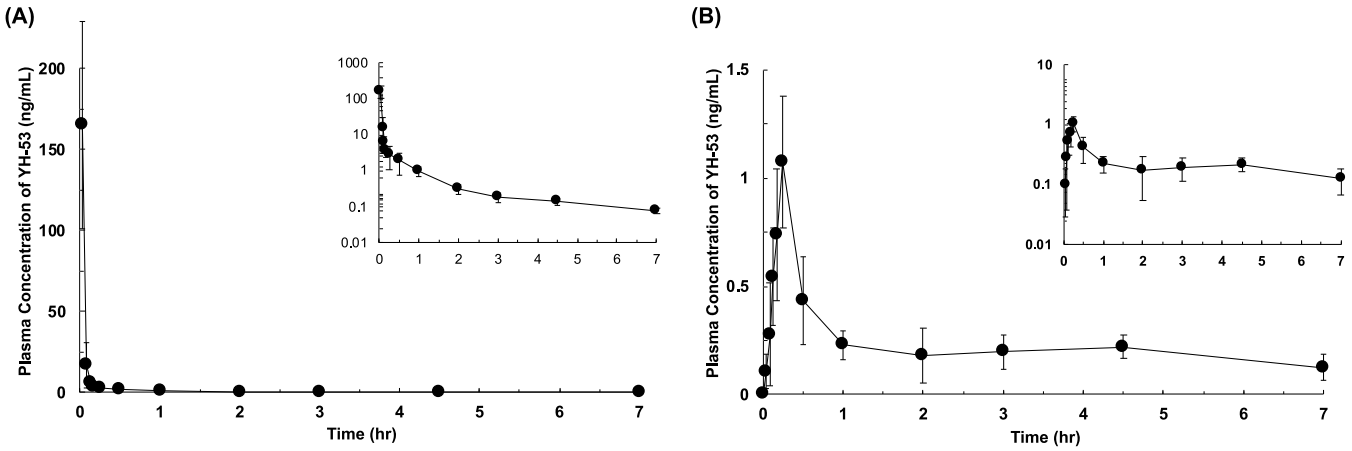

Figure 5. Mean plasma concentration−time profile of YH-53 in rats. (A) Mean plasma concentration−time profile of YH-53 in rats after i.v. administration. YH-53 (0.1 mg/kg; 4 mL/kg) was administered by an i.v. bolus injection in rats. Inset depicts the same data on a semilogarithmic scale. Data are shown as the mean ± SD (n = 5). (B) Mean plasma concentration−time profile of YH-53 in rats after oral administration. YH-53 (0.5 mg/kg; 4 mL/kg) was administered orally in rats. Inset depicts the same data on a semilogarithmic scale. Data are shown as the mean ± SD (n = 5).

region. Notably, the observed conformational change of the loop region is rather rare among the 3CL^{pro} structures that have been characterized to date. Of the 345 3CL^{pro} coordinates that were selected with RMSD values less than 2.0 Å for the YH-53 complex, only 12 structures have similar conformations of the loop region (Figure 3F).

Antiviral Activity of SH-5, YH-53, and YH-71. The antiviral activities of the inhibitors SH-5, YH-53, and YH-71 against SARS-CoV-2 were examined by a cytopathic effect (CPE) assay in Vero cells. As shown in Figure 4A, the viral proliferation was completely blocked by the addition of 25 μM SH-5, YH-53, or YH-71. Unlike the recombinant 3CL^{pro} inhibition, YH-53 showed better antiviral activity than SH-5. Of note, YH-53 completely blocked the viral proliferation even at a concentration of 10 μM. No cytotoxicity of YH-53 was observed with a CC_{50} value of >100 μM (Figure S4). To further validate the antiviral effect of YH-53, we used a quantitative real-time polymerase chain reaction (qRT-PCR) to monitor the total amount of viral RNA (Figure 4B). Consistent with the CPE assay, copies of total RNA were efficiently reduced with increased concentrations of YH-53. The antiviral activity of YH-53 was enhanced by adding CP-100356, which is a potent inhibitor of MDR-1 efflux transporter (Figure S5). These results indicate that YH-53 is a potent antiviral agent against SARS-CoV-2.

Computational and *In Vitro* Safety and Toxicity Profiling of YH-53. Encouraged by these results, we turned our attention to the possibility of YH-53 having drug development potential. First, we studied the behavior of YH-53 in plasma. YH-53 was found to be significantly stable in plasma, and no degradation was observed at 37 °C for 6 h in rat plasma. It was observed that 99% of YH-53 bound to the plasma proteins in both human and rat plasma. Next, we investigated the *in vitro* safety and toxicity profile of YH-53. To assess CYP inhibition by YH-53, human microsomes were incubated with YH-53 and the activity of CYP1A2, CYP2C8, CYP2C9, CYP2D6, and CYP3A4 was measured. As shown in Table S2, no CYP2C9 and CYP3A4 inhibition of YH-53 was observed, while CYP1A2, CYP2D6, and CYP2C8 were moderately inhibited at 10 μM YH-53, which is considered tolerable. To examine the mutagenicity of YH-53, the Ames test and the MicroFlow assay were conducted. YH-53 showed no mutagenetic activities for both *Salmonella typhimurium* TA98 and TA100 strains and did not induce formation of micronuclei. We

https://doi.org/10.1021/acs.jmedchem.1c00665
J. Med. Chem. XXXX, XXX, XXX−XXX

also tested YH-53 in a hERG inhibition assay to assess potential cardiotoxicity. No inhibition of the hERG current was observed at >100 μM of YH-53. In another approach to validation of the feasibility of a possible drug based on YH-53, we analyzed its pharmaceutical properties using an informatics method.[35] Construction of chemical space and a subsequent principal component analysis (PCA) revealed that YH-53 was mapped onto the same region occupied by other FDA-approved small molecule drugs (Figure S6).[36] Specifically, the location of YH-53 was within the distribution range of antiviral protease inhibitors, known as the -navir group. Taken together, these results suggest that YH-53 possesses a favorable safety profile as a potential drug.

Preclinical *In Vitro* and *In Vivo* Assessment of ADME/PK Properties of YH-53. To characterize and understand the ADME properties of YH-53, its oral bioavailability and pharmacokinetics in rats were assessed with various *in vitro* and *in vivo* experiments. When YH-53 (0.1 mg/kg) was intravenously administered to rats, the area under the plasma concentration−time curve ($AUC_{0-\infty}$) of YH-53 was evaluated as 19.7 ± 8.2 ng·h/mL (Figure 5A and Table 1). After oral administration at 0.5 mg/kg, the $AUC_{0-\infty}$ of YH-53 was 3.49 ± 1.00 ng·h/mL in rats (Figure 5B and Table 1). Based on these pharmacokinetic parameters, the absolute bioavailability (BA) of YH-53 in rats was estimated to be 3.55% (Table 1). The maximum plasma concentration (C_{max}) and the time to reach maximum plasma concentration (t_{max}) of YH-53 were 1.08 ± 0.30 ng/mL and 0.350 ± 0.137 h, respectively. Interestingly, a higher apparent distribution volume of YH-53 (V_d = 3.51 ± 2.83 L/kg) subsequent to intravenous infusion was observed, suggesting a high peripheral distribution into body tissues. This is supported by the results from compartmental analysis demonstrating that the pharmacokinetic data could be best fitted to the three-compartment model based on the lowest value of the Akaike Information Criterion (18.2, 13.2, −30.2, and −26.2 for the one, two, three, and four compartment models, respectively) (Figure S7 and Table S3). On the other hand, the terminal half-life ($t_{1/2}$) of YH-53 after intravenous administration was 2.97 ± 1.02 h, while $t_{1/2}$ of YH-53 after oral administration was 9.64 ± 6.11 h, results that appear to be inconsistent. In Table S4, the permeability of YH-53 (1 μM) was assessed using monolayers of Caco-2 cells and exhibited high permeability values ($18.9 \pm 1.1 \times 10^{-6}$ cm/s). Moreover, *in vitro* metabolism study of YH-53 using cryopreserved hepatocytes in human and rat led to the identification of seven metabolites, and the main metabolic pathway appeared to be amide hydrolysis, producing HC-5, HC-6, and HC-7, with lesser contributions from cytochrome P450 (CYP)-catalyzed oxidative pathways (Figure S8 and Table S5).

Table 1. Pharmacokinetic Parameters of YH-53 in Rats after Intravenous and Oral Administration[a]

pharmacokinetic parameters[b]		i.v.[c]	oral[d]
dose	(mg/kg)	0.100	0.500
C_{max}	(ng/mL)		1.08 ± 0.30
t_{max}	(h)		0.350 ± 0.137
AUC_{0-7}	(ng·h/mL)	19.3 ± 8.2	1.59 ± 0.38
$AUC_{0-\infty}$	(ng·h/mL)	19.7 ± 8.2	3.49 ± 1.00
$t_{1/2}$	(h)	2.97 ± 1.02	9.64 ± 6.11
MRT_{tot}	(h)	0.494 ± 0.147	13.2 ± 7.6
CL_{tot}	(L/h/kg)	6.43 ± 3.50	
CL_{tot}/F	(L/h/kg)		159 ± 70
V_d	(L/kg)	3.51 ± 2.83	
V_d/F	(L/kg)		1800 ± 773
F	(%)	3.55	

[a]YH-53 was intravenously (0.1 mg/kg) and orally (0.5 mg/kg) administered to rats. [b]Definitions of disposition parameters: $AUC_{0-\infty}$, area under plasma concentration−time curve from 0 to infinity; C_{max}, peak plasma drug concentration; t_{max}, time to reach maximum plasma concentration; CL_{tot}, total clearance; F, oral bioavailability; V_d, volume of distribution; $t_{1/2}$, elimination half-life. [c]Pharmacokinetic parameters of YH-53 after a single intravenous dose were obtained from Figure 1. [d]Pharmacokinetic parameters of YH-53 after a single oral dose were obtained from Figure 2. Data are shown as means ± SD (n = 5).

DISCUSSION

Protease inhibitors are major therapeutic agents for viral infections involving HIV and hepatitis C virus. In general, the design of these inhibitors is based on the natural substrate structure and introducing the appropriate inhibitory machinery that adapts to the substrate degradation mechanism of the protease. Similarly, drug development targeting the $3CL^{pro}$ of SARS-CoV-2, a cysteine protease, is a promising strategy to fight COVID-19. In this report, we investigated the inhibitory effect of our original substrate-derived SARS-CoV-1 $3CL^{pro}$ inhibitors SH-5, YH-53, and YH-71 against SARS-CoV-2. All three inhibitors containing benzothiazolylketone, a unique P1′-arylketone moiety, showed potent inhibition against SARS-CoV-2 $3CL^{pro}$ and completely blocked the viral proliferation at 25 μM in Vero cells (Figures 2A and 3A, B). The $TCID_{50}$ value of the most potent YH-53 was ∼5 μM. Our data suggests that aryl ketone-type $3CL^{pro}$ inhibitors developed for SARS-CoV-1 are effective against SARS-CoV-2 with a clear mechanism of action in a competitive manner. The results are largely attributed to the quite high similarity in the entire amino acid sequence and three-dimensional structure, particularly 100% identity at the active site in $3CL^{pro}$ between SARS-CoV-1 and SARS-CoV-2.[2,29] NMR data also indicated that this specific binding of YH-53 with $3CL^{pro}$ is 1:1 stoichiometry with slow exchange kinetics, suggesting that the binding is tightly maintained (Figure S2). The potent anti-SARS-CoV-2 activity of YH-53 is consistent with a recent report by Hattori et al.[29] It should be noted, however, that a slight gap was observed between the enzyme inhibitory and antiviral activities. This may be due to the ineffectiveness of the inhibitors to either penetrate into the cell or achieve high concentrations owing to the decomposition, consumption, or exclusion from the cell. In the MDR1 substrate screening assay, YH-53 acts as a substrate of the p-glycoprotein efflux pump (basal to apical/apical to basal ratio > 130) that is also expressed in Vero cells,[37] and this could be a valid reason for consumption of high concentrations of inhibitors to realize the effective *in vitro* antiviral activity (Figure S4). It has been reported that the expression level of the MDR1 gene increased by inflammatory responses in COVID-19 patients with mild or severe symptoms.[38] However, the upregulation of MDR1 expression is limited to a small subset of respiratory cells and most respiratory cells remain MDR1 negative.[38] Further in vivo studies on the antiviral activity of YH-53 need to be pursued.

In an effort to understand the precise recognition of arylketone-type $3CL^{pro}$ inhibitors, high resolution X-ray structures of SARS-CoV-2 $3CL^{pro}$-YH-53 and -SH-5 complexes were established (Table S1, Figure 3A and B). In addition to the key interactions between P1 pyrrolidine-2-one and Glu166 and His163, heteroatoms of benzothiazole at P1' form further

https://doi.org/10.1021/acs.jmedchem.1c00665
J. Med. Chem. XXXX, XXX, XXX−XXX

hydrogen bonds with water and His41, which would contribute the tight binding of the inhibitors. It has been observed that each side chain moiety on the extended conformation of YH-53 and SH-5 backbones fits into each substrate pocket in the active site of $3CL^{pro}$, and it was proven that the tight binding of these high-affinity inhibitors leads to the potent enzyme inhibitory activity with K_i values in the low nanomolar range. Interestingly, at the N-terminal part where the structure of two inhibitors is different, the binding mode to the protease was different (Figure 3D and E). Compared to the tripeptide-type SH-5 containing the P4 part, the smaller dipeptide-type YH-53 resulted in a significant conformational change of the loop region of $3CL^{pro}$, drawing it closer to the inhibitor and making the active site more closed. This explains the strong interaction of YH-53 with $3CL^{pro}$ even in the absence of the P4 moiety. It has also been revealed that this characteristic conformational change of the loop region is rare, as shown by the comparison with known PDB coordinates of $3CL^{pro}$ (Figure 3F). Other inhibitor-$3CL^{pro}$ complexes keep the loop structures similar to the inhibitor free form. Therefore, the conformational change may be a useful indicator for assessing the properties of new inhibitors developed in the future.

Safety and toxicological evaluations suggested that the most potent antiviral $3CL^{pro}$ inhibitor YH-53 has a high safety index with low cytotoxicity, no or moderate but tolerable CYP inhibition, no mutagenicity and no cardiotoxicity (Table S2). As mentioned above, YH-53 was identified as the best SARS-CoV-2 $3CL^{pro}$ inhibitor in the screening of a compound library of 400 potential inhibitors which found YH-53 to be an excellent lead compound with a favorable safety profile.[29] Physicochemical properties including values of molecular weight of 575, cLogP of 2.37, LogD of 3.37, kinetic solubility of 7.7 μg/mL, and PAMPA of 213 nm/s are in the acceptable range for lead candidates. Moreover, the computational analysis reveals that YH-53 has strong potential for drug development, endowed with similar pharmaceutical properties to existing clinically used antiviral protease inhibitors (Figure S6).

By means of the simultaneous analysis of intravenous and oral pharmacokinetic data, the bioavailability of YH-53 in rats was estimated to be approximately 3.6% (Table 1). This low bioavailability is caused by poor absorption and/or significant first-pass metabolism. Interestingly, *in vitro* assessment of intestinal permeability of YH-53 using a Caco-2 cell monolayer system exhibited excellent permeability, close to that of metoprolol, a completely absorbed drug (Fa $\geq$ 90%) (Table S4). Moreover, an *in vitro* metabolism study revealed that YH-53 is mainly metabolized by hydrolytic enzymes, with minor contributions from CYP enzymes (Figure S8 and Table S5). Taking these results into account, it is reasonable to consider that the low bioavailability of YH-53 in rats may be mainly due to the first-pass metabolism catalyzed by hydrolytic enzymes such as carboxylesterases or proteases in the intestine and/or liver. Meanwhile, a higher apparent distribution volume of YH-53 than the total body water (0.668 L/kg) of rats was observed, suggesting a high peripheral distribution into body tissues.[39] This is emphasized by the fact that the pharmacokinetic data were best fitted to the three-compartment model. Theoretically, a three-compartment model raises the possibility that there is an initial fast distribution phase (fast-redistributing tissues) and slow distribution phase (slow-redistributing tissues), followed by an elimination phase based on redistribution from drug stored in the tissues. Further investigation would be necessary to examine the distribution of YH-53 to potential target organs such as lung, bronchial airway, intestine, heart, liver, and kidney which express angiotensin-converting enzyme 2 (ACE2), a functional receptor for SARS-CoV-2 infection. On the other hand, the $t_{1/2}$ value of YH-53 after intravenous administration was approximately 3 h, indicating its relatively fast elimination from the body; that is, the mean residence time (MRT) in plasma is limited. However, after oral administration, the $t_{1/2}$ value of YH-53 was approximately 10 h, implying a prolonged elimination of YH-53. These inconsistent observations of intravenous and oral administrations may be explained by apparent flip-flop kinetics due to irregular absorption of YH-53. Indeed, the plasma concentration−time profile after oral administration shown in Figure 5B seems to exhibit the unexpected double peaks, a moderate extra peak. At present, the precise mechanism expressing the double peak in the plasma concentration−time profile after oral administration of YH-53 is not totally clear, but speculation is that this phenomenon may be caused by irregular absorption due to the enterohepatic recirculation, site-specific absorption, variable gastric emptying, or precipitation/resolubilization in the gastrointestinal tract. Further studies will be needed to clarify the mechanisms of a large difference in the $t_{1/2}$ value of YH-53 between intravenous and oral administrations. Our finding will help to design and develop the more potent inhibitors with excellent pharmacokinetic profiles.

PF-00835231, which is one of the most advanced $3CL^{pro}$ inhibitors, independently developed by the Pfizer group, has a similar chemical structure as YH-53[40] While YH-53 contains a benzothiazolylketone group as the warhead, PF-00835231 has a hydroxymethylketone at the corresponding position. Both compounds showed similar antiviral activities and low cytotoxicity (CC_{50} > 100 μM) and are recognized by MDR-1. Hence, the antiviral activity of both compounds is enhanced under the presence of an MDR-1 inhibitor. Compared with the oral bioavailability of PF-00835231 (1.4%), that of YH-53 (3.6%) is in the same range.[37] The higher cLogP value of YH-53 (2.37) compared with PF-00835231 (0.75) would be due to the increased hydrophobicity of the benzothiazole unit, which may contribute to the relatively long $t_{1/2}$ (9.6 h) of YH-53 compared with the $t_{1/2}$ of PF-00835231 (0.72 h) after oral administration. This relatively high hydrophobicity is also contributing to the high cell penetration propensity of YH-53. These results indicate that YH-53 can be a valuable lead compound with a different warhead group

CONCLUSION

In conclusion, YH-53, our original $3CL^{pro}$ inhibitor of SARS-CoV-1, is a potential lead compound for the development of an anti-COVID-19 drug. YH-53 exhibited not only potent SARS-CoV-2 inhibition in $3CL^{pro}$ and cellular antiviral assays but also a most favorable *in vitro* ADME profile. *In vivo* pharmacokinetics and metabolic analyses of YH-53 indicated that the first pass effect with hydrolysis between the P1−P2 amide bond in the liver would be the main reason of the low bioavailability of YH-53 in rats. We believe that these data will strongly facilitate the drug development targeting SARS-CoV-2 $3CL^{pro}$.

EXPERIMENTAL SECTION

General Part. The purity of SH-5, YH-53, and YH-71 exceeded 95% by HPLC analysis. The analytical HPLC charts are disclosed in the Supporting Information.

https://doi.org/10.1021/acs.jmedchem.1c00665
J. Med. Chem. XXXX, XXX, XXX−XXX

Preparation of SH-5, YH-53, and YH-71. SH-5,[25] YH-53,[27] and YH-71[27] were synthesized and purified according to published procedures.

Expression and Purification of SARS-CoV-2 3CL^{pro}. For the enzyme inhibition assay, the full-length SARS-CoV-2 3CL^{pro}, His-tagged at the C-terminus, was expressed and purified as described previously.[28] For crystallization, the SARS-CoV-2 3CL^{pro}-encoding pGEX-6P-1 vector was kindly provided by Dr. Rolf Hilgenfeld.[12] Briefly, *E. coli* BL21 (DE3) transformed with the plasmid was precultured in 5 mL of LB medium supplied with ampicillin (100 μg/mL) at 37 °C overnight. The incubated culture was inoculated into 1 L of LB medium supplied with 100 μg/mL ampicillin. The cells were induced with 0.5 mM isopropyl-D-thiogalactoside (IPTG) until the OD_{600} reached 0.6−0.8. After incubation for 5 h at 30 °C, the cells were harvested by centrifugation at 2000*g*, 4 °C for 30 min. The pellets were resuspended in 30 mL of the lysis buffer (20 mM Tris, 150 mM NaCl, pH 7.8) and then lysed by sonication on ice. The lysate was clarified by centrifugation at 10 000*g* at 4 °C for 1 h. The supernatant was loaded onto a HisPurTM Ni-NTA resin (Thermo Scientific) which was equilibrated with the lysis buffer. The resin was washed with the lysis buffer with 10 mM imidazole to remove nonspecifically binding proteins, followed by elution with imidazole ranging from 20 to 400 mM. The fractions containing the target protein were combined and mixed with PreScission protease (Cytiva) at a molar ratio of 5:1 and dialyzed into the dialysis buffer (20 mM Tris, 150 mM NaCl, 1 mM DTT, pH 7.8) at 4 °C overnight, resulting in the target protein with authentic N- and C-termini. The PreScission-treated 3CL^{pro} was applied to connected GST-Accept (Nacalai Tesque Inc.) and HisPurTM Ni-NTA resin to remove the GST-tagged PreScission protease, the His-tag, and the protein with uncleaved His-tag. The His-tag-free 3CL^{pro} in the flow-through was subjected to buffer exchange with the stock buffer (20 mM Tris, 150 mM NaCl, 1 mM EDTA, 1 mM DTT, pH 7.8) by using Amicon Ultra 15 centrifugal filters (10 kDa, Merck Millipore) at 3000*g* at 4 °C. The purified 3CL^{pro} (10 mg/mL) was stored at −80 °C and used for crystallization.

SARS-CoV-2 3CL^{pro} Inhibition Assay. Recombinant His-tagged SARS-CoV-2 3CL^{pro} was defrosted and used immediately in the enzyme assays which were performed on a Pherastar FSX plate reader (BMG Labtech, Offenburg, Germany) at 37 °C with an excitation wavelength of 360 nm and an emission wavelength of 460 nm. Black half area 96-well plates with a flat bottom were obtained from Greiner Bio-One (Kremsmünster, Austria). The assay buffer was 50 mM 3-(*N*-morpholino)propanesulfonic acid (MOPS), pH 7.2 containing 10 mM NaCl, 1 mM EDTA, and 0.01% Triton X-100. A 2.5 mM stock solution of the substrate (Boc-Abu-Tle-Leu-Gln-AMC)[28] was prepared in DMSO. Test compounds were dissolved in DMSO to obtain 1.0 mM stock solutions. The substrate was diluted 33-fold with assay buffer and pipetted into a well containing 1 μL of inhibitor solution. This mixture was incubated at 37 °C for 5 min. Upon addition of 1 μL of enzyme solution (0.4 μg/μL His-tagged 3CL^{pro} diluted in 14 μL of assay buffer), the measurement was started and recorded for 10 min. The final enzyme concentration was 8 ng/μL of His-tagged 3CL^{pro}. The final substrate concentration was 50 μM which approximately corresponds to its K_m value, and the final DMSO concentration was 4%. The product formation rate of the uninhibited control was set at 100%. At least 11 different inhibitor concentrations were tested to determine IC_{50} values. The product formation rate during the first 10 min was evaluated and plotted versus the corresponding inhibitor concentrations. IC_{50} values were calculated by nonlinear regression. The corresponding K_i values were calculated using the Cheng−Prusoff equation.[41] The inhibition type of SH-5 was determined by monitoring the effects of five different inhibitor and substrate concentrations on the product formation rate for 10 min. The inhibition type of SH-5 was determined by monitoring the reactions for 10 min in the presence of five different inhibitor and substrate concentrations. The Lineweaver−Burk plot and the global data fitting for competitive inhibition were performed with GraphPad Prism 8.0.

Crystallization of SARS-CoV-2 3CL^{pro}-YH-53 and -SH-5. The crystallization conditions of the 3CL^{pro}-YH-53 complex were initially screened using Crystal Screen 1 and 2 (Hampton Research) and PEGsII (Qiagen) with a Protein Crystallization System 2 (PXS2) at the Structural Biology Research Center, KEK in Japan.[42] Screening was performed by the sitting-drop vapor-diffusion method with crystallization drops consisting of 0.2 μL protein solutions (4.6 mg/mL 3CL^{pro} containing 0.9 mM YH-53) and 0.2 μL screening solutions at 277 K. Crystals of the 3CL^{pro}-YH-53 complex were observed after 3 days under the conditions of Crystal Screen 1 #10 (30%(w/v) PEG4000, 0.2 M ammonium acetate, 0.1 M sodium acetate pH 4.6) at 277 K. Crystallization conditions were further optimized, and the final crystallization conditions were 25% (w/v) PEG4000, 0.2 M ammonium acetate, and 0.1 M sodium acetate at pH 4.6. Before diffraction data collection, crystals were cryoprotected in a solution containing 30% (v/v) ethylene glycol, 25% (w/v) PEG4000, 0.14 M ammonium acetate, and 70 mM sodium acetate at pH 4.6 for 20 s. Crystallization conditions of the 3CL^{pro}-SH-5 complex were optimized based on the crystallization conditions of the 3CL^{pro}-YH-53 complex by the sitting-drop vapor-diffusion method with crystallization drops consisting of 1.2 μL protein solutions (4.6 mg/mL containing 0.9 mM SH-5) and 1.2 μL screening solutions at 277 K by varying the concentration of PEG4000. The final crystallization conditions were 17.5% (w/v) PEG4000, 0.2 M ammonium acetate, and 0.1 M sodium acetate at pH 4.6. Before diffraction data collection, crystals were cryoprotected in a solution containing 30% (v/v) ethylene glycol, 25% (w/v) PEG4000, 0.14 M ammonium acetate, and 70 mM sodium acetate at pH 4.6 for 20 s. X-ray diffraction data were collected at 95 K, using an Eiger X16 M detector on BL-17A of the Photon Factory, KEK (Tsukuba, Japan). Diffraction data were processed and scaled by XDS and XSCALE, respectively.[43] The phases were determined by the molecular replacement method[44] using the program Phaser with the previously reported model of 3CL^{pro} (PDB ID: 6Y2F) as a search model. Refinement of the crystallographic was performed using PHENIX.refine[45] and Coot.[46]

NMR Interaction Study between SARS-CoV-2 3CL^{pro} and YH-53. For the NMR study, a double-stranded DNA fragment encoding N-terminal NH-tagged SARS-CoV-2 3CL^{pro} was synthesized (Thermo Fisher Scientific) with a PreScission protease sequence located between NH-tag and the target protein. The DNA fragment was subjected to a 16 h *in vitro* translation with stable isotope labeled amino acids for Met-ε1 $^{1}H,^{13}C$-labeling under a ^{2}H-labeling background (Musaibou-kun, Taiyo Nippon Sanso). The resultant reaction solution containing NH-tagged SARS-CoV-2 3CL^{pro} was purified for crystallization in the same way as the *E. coli* expressed SARS-CoV-2 3CL^{pro}. YH-53 titration experiments were performed using a Bruker Avance-600 MHz spectrometer equipped with cryogenic triple resonance probes (Bruker Biospin). NMR experiments were performed at 298 K and TOPSPIN (Bruker Biospin) was used to process NMR spectra.

SARS-CoV-2 Antiviral Assay. Vero cells were seeded onto 96-well plates at 1.0×10^4 cells/well and cultured at 37 °C overnight. Viruses (KNG strain) were used to inoculate cell line at MOI = 0.01. After adsorption at 37 °C for 1 h, the cells were washed with DMEM and with fresh DMEM containing 10% FBS with different concentrations of SH-5, YH-53, and YH-71. Infected cells were cultured at 37 °C for 72 h, and culture supernatants were collected to determine infectious virus titers using $TCID_{50}$. For $TCID_{50}$, viruses were diluted by 10-fold serial dilution from 10 times dilution using DMEM without FBS. The diluted viruses were inoculated into Vero cells and incubated at 37 °C for 4 days. After incubation, the infected cells were fixed with buffered formaldehyde (Nacalai Tesque) and stained with crystal violet. The $TCID_{50}$ was calculated by the Spearman and Karber algorithm.

Cytotoxic Assay. Vero cells were seeded onto 96-well plates at 1.0×10^4 cells/well and cultured at 37 °C overnight. SH-5, YH-53, and YH-71 were individually added to the cultured Vero cells. After incubation for 24 h, MTT assays were carried out using the MTT Cell Count Kit (Nacalai Tesque) according to manufacturer's instructions. Absorbance at 570 nm was then measured with the iMark microplate absorbance reader (BioRad).

SARS-CoV-2 Antiviral Assay with a MDR-1 inhibitor. VeroE6/TMPRSS2 cells were seeded onto 12-well plates at 1.0×10^5 cells/well and cultured at 37 °C overnight. Cells were infected with SARS-CoV-2 virus (JPN/TY/WK-521 strain) at MOI = 0.1. After adsorption at 37

https://doi.org/10.1021/acs.jmedchem.1c00665
J. Med. Chem. XXXX, XXX, XXX−XXX

°C for 1 h, the cells were washed with DMEM and fresh DMEM containing 10% FBS with different concentrations of YH-53 and CP-100356. At 24 h postinfection, the culture supernatants were collected and the viral genomes were purified using the MagMax Vrial/Pathogen Nucleic Acid Isolation Kit (Thermo Fisher Scientific). The level of viral genomes was determined by real time RT-PCR with SuperScript III (Thermo Fisher Scientific) and FastStart SYBR Green Master (Roche) using primers specific for *S* gene (5′-CAATGGTTTAACAGGCAC-AGG-3′ and 5′-CTCAAGTGTCTGTGGATCACG-3′).

Rat Plasma Stability. YH-53 (1 μM) was added into the plasma and incubated at 37 °C for 0, 1, 2, and 6 h. After incubation, the compound concentrations in the plasma were determined by LC/MS/MS (UFLC system coupled to an API 4000 triple quadrupole mass spectrometer and Unison UK-C18 HT column (3.0 μm, 2.0 × 20 mm)).

Plasma Protein Binding. Human donor-pooled plasma was purchased from Cosmo Bio Co. Ltd. (Tokyo, Japan). Rat plasma used in the study was obtained from Crl:CD(SD) (IGS) male rats (Charles River Laboratories Japan, Inc., Kanagawa, Japan). The plasma protein binding of each compound was determined by the equilibrium dialysis method with HTDialysis Teflon dialysis chambers and cellulose membranes (MWCO 6−8 kDa). Human and rat plasma were mixed with YH-53 (1 μM). Dialysis was conducted against PBS in an 8% CO_2-supplemented atmosphere at 37 °C for 16−20 h. The concentrations of the compound in both plasma and PBS were determined by LC/MS/MS (UFLC system coupled to a Triple QUAD 5500 (SCIEX, MA) and Unison UK-C18 HT column (3.0 μm, 2.0 × 20 mm)). The unbound fraction in plasma (fu, p) was calculated as the ratio of the peak area of compounds from PBS side to those from the plasma side of the dialysis apparatus.

Kinetic Solubility. YH-53 solution dissolved in DMSO was added to the second fluid for the disintegration test of the Japanese Pharmacopoeia (JP2nd). After incubation, precipitates were separated by filtration. The solubility was determined by using a UV plate reader (SpectraMax 384plus, Molecure device, CA).

CYP Inhibition Assay. Human liver microsomes were purchased from Sekisui XenoTech, LLC. The microsomes (0.1 mg protein/mL), substrates (tacrine, paclitaxel, tolbutamide, dextromethorphan, and midazolam, respectively), and YH-53 (10 μM) were mixed in phosphate buffer (pH 7.4). The reactions were initiated by adding an NADPH generating system (a mixture of $MgCl_2$, β-$NADP^+$, glucose-6-phosphate, and glucose-6-phosphate dehydrogenase) to the mixtures before incubation. The mixture was incubated at 37 °C for 10 min, and the reaction was terminated by adding acetonitrile. The activities of CYP1A2, CYP2C8, CYP2C9, CYP2D6, and CYP3A4 were determined by the peaks of 1-hydroxytacrine, 6α-hydroxypaclitaxel, 4-hydroxytolbutamide, dextrorphan, and 1′-hydroxymidazolam, respectively. The analysis was conducted by LC/MS/MS (UFLC system coupled to an API 5000 triple quadrupole mass spectrometer and Unison UK-C18 (3.0 μm, 2.0 × 10 mm)). The activities of test samples were expressed as the percentage of activity remaining compared with a control sample containing no inhibitor. The inhibition ratio (% inhibition) was calculated to the following:

$$\{1 - (\text{activity with test compound})/(\text{activity with vehicle})\} \times 100$$

Principal Component Analysis. To construct the chemical space, SD (Structure-Data) files of 2034 FDA-approved drugs were downloaded from DrugBank[36] (assessed July 2, 2020). In order to distinguish various kinds of protease inhibitors from the other drugs, 15 gliptin group drugs (alogliptin, anagliptin, bisegliptin, carmegliptin, evogliptin, gemigliptin, gosogliptin, linagliptin, omarigliptin, retagliptin, saxagliptin, sitagliptin, teneligriptin, trelagliptin and vildagliptin), 26 pril group (benazepril, benazeprilat, captopril, cilazapril, cilazaprilat, delapril, enalapril, enalaprilat, epicaptopril, fosinoprilat, imidapril, lisinopril, moexipril, moexiprilat, perindopril, perindoprilat, quinapril, quinaprilat, ramipril, ramiprilat, spirapril, tempcapril, trandolapril, trandolaprilat, zofenopril and zofenoprilat), one previr group (bioceprevir) and 8 navir group drugs (amprenavir, darunavir, denavir, fosamprenavir, indinavir, mozenavir, nelfinavir and tipranavir) were extracted. An SD file of YH-53 was also produced by Avogadro.[47] Fourteen physicochemical properties used as chemistry informer descriptors[35] were calculated from the SD files by RDKit (Open-Source Cheminformatics Software). PCA was carried out by scikit-learn (Open-Source Machine Learning Libraries). The resulting chemical space was presented on the projective plane composed of the first (PC1) and the second (PC2) principal component axes for evaluation.

Ames Test. *Salmonella typhimurium* TA98 and TA100 were originally transferred from National Institute of Technology and Evaluation (Tokyo, Japan) and were subsequently maintained in-house. Two Ames Salmonella tester strains were used: TA98, which detects frameshift mutations, and TA100, which detects base pair substitutions. Briefly, each tester strain was preincubated for 20 min both with and without a phenobarbital and 5,6-benzoflavone-induced rat liver S9 fraction (IEDA Trading Corporation, Tokyo, Japan) in duplicate in 96-well plates with six concentrations (1.4−333.3 μg equiv/well) of each compound. Six concentrations of each positive control mutagen (in duplicate) and 12 replicates of vehicle controls (DMSO, FUJIFILM Wako Pure Chemical Corporation, Osaka, Japan) were also used. The positive control without S9 was 2-(2-furyl)-3-(5-nitro-2-furyl) acrylamide (Oriental Yeast Co., Ltd., Tokyo, Japan). The positive control with S9 was 2-aminoanthracene (Oriental Yeast Co., Ltd.). After preincubation, semienriched top agar was added to the 96-well plate and mixed sufficiently, and then the mixtures were overlaid on minimal glucose agar 24-well plates. After the overlaid agar solidified, these plates were stored at 37 °C in an incubator (MIR-553, Sanyo Electric Biomedical Co., Ltd., Osaka, Japan) for 48 h. Cultures were examined for signs of cytotoxicity (decreased background lawn), compound precipitation, and number of mutant colonies. Revertant colonies in each well were counted with an automatic colony counter (Gelcounttm, Oxford Optronix Ltd., Abingdon, United Kingdom). A positive response was defined as the appearance of ≥2-fold revertant colonies for TA100 and ≥3-fold for TA98 over the control revertant colonies. As an additional criterion used, an average of at least nine colonies for TA100 or six colonies for TA98, and concentration−response relationships were also taken into account to consider a compound positive in this assay.

hERG Assay. Whole-cell patch-clamp voltage clamp experiments were performed on Chinese hamster ovary cells lines stably expressing the human ether-a-go-go related gene (CHO hERG Duo, B'SYS GmbH, Witterswil, Switzerland). Measurements were performed using a SyncroPatch 384PE (Nanion Technologies, Munich, Germany) incorporated into a Biomek FX pipetting robot (Beckman Coulter, CA), and ×4 hole chips with high resistance (Nanion, NPC R-384 patchclamp 4 × High) were used. The external solution consisted of 10 mM HEPES, 140 mM NaCl, 4 mM KCl, 1 mM $MgCl_2$, 2 mM $CaCl_2$, and D-glucose 5 mM and was adjusted to pH 7.4 with NaOH. The internal solution contained 10 mM HEPES, 120 mM KF, 20 mM KCl, 10 mM EGTA and was adjusted to pH 7.2 with KOH. hERG current was measured using a pulse pattern, repeated every 5 s, consisting of a depolarization to 40 mV for 500 ms, followed by a ramp (−1.2 V/s) to −80 mV for 100 ms (holding potential = −80 mV). Peak tail current was measured during the repolarizing ramp. All experiments were performed at room temperature (rt), while the cell suspension was rotated at 4 °C on a Peltier shaker (CellHotel) until use. Concentration response curves for each compound were investigated independently, *i.e.*, each cell received only one compound, typically increasing concentrations of 1.1, 3.3, 10, and 30 μM in a cumulative fashion with a 5 min interval. To monitor the current stability during the compound period, some cells received vehicle control (0.3~0.4% (v/v) DMSO) instead. Positive control (0.11, 0.33, 1, and 3 μM of verapamil) and negative control (0.3, 0.3, 0.3, and 0.4% (v/v) DMSO) values were measured in each plate. Valid whole-cell recordings had to meet the following criteria: (i) a seal resistance ≥ 50 MΩ for a multihole (4 cells) patch clamp experiment, (ii) peak current ≥ 0.5 nA, and (iii) run-down or -up during before drug application: within ±10%. or in the DMSO control (whole experimental period): within ±15%.

***In Vitro* MicroFlow Assay.** The precultured human lymphoblastoid TK-6 cells (DS Pharma Promo Co., Ltd., Osaka, Japan) resuspended in assay culture medium were plated on 96-well plates. Then, for the short-term treatment group with metabolic activation, the

https://doi.org/10.1021/acs.jmedchem.1c00665
J. Med. Chem. XXXX, XXX, XXX−XXX

cells were treated with test compound and 1% (v/v) + S9 mixture for 3 h followed by a further 21 h incubation in a humid atmosphere at 37 °C with 5% CO_2 (PHC Corporation, Tokyo, Japan) without test compound and S9 mixture. For the continuous treatment group without metabolic activation, the cells were incubated with test compound without S9 mixture for a continuous 24 h in the humid atmosphere at 37 °C with 5% CO_2. Cyclophosphamide (CP, for treatment with metabolic activation, Shionogi & Co. Ltd. Osaka, Japan) and Mitomycin C (MMC, for treatment without metabolic activation, Kyowa Hakko Kirin Co. Ltd., Tokyo, Japan) were used as concurrent positive controls to ensure the performance of the assay. After treatment, the cells were washed and stained according to the package insert of In Vitro MicroFlow Kit and measured with the BD LSR Fortessa (Becton, Dickinson and Company). Briefly, cells were first stained with a photoactivated dye, Dye A (EMA) and then washed, lysed, and stained with lysis solutions containing RNase, nucleic acid Dye B (SYTOX Green), and counting beads. DNA from apoptotic/necrotic cells with compromised cell membranes was labeled with both EMA and SYTOX Green, which can be distinguished from EMA-negative and SYTOX Green-positive MN. Measurements were performed on 20 000 main nuclei per concentration. If there were less than 10 000 main nuclei per concentration, this was recorded in the "remarks" column. The micronucleus was set at 1/100 to 1/10 of the 2*n* nuclear fluorescence intensity. The lowest concentration at which precipitation was observed at the end of the treatment was adopted as the highest evaluation concentration. As the same amount of counting beads was added to each well, the nuclei to beads ratio was used to calculate relative population doubling (RPD) as a cytotoxicity measurement. The relative population doubling (RPD) at each concentration were calculated by the following formulas.

$$\mathrm{PD} = \log([\text{final number of main nuclei}]/[\text{starting number of main nuclei}])/\log 2$$

$$\mathrm{RPD}\ (\%) = (\text{PD in the test article treated group})/(\text{PD in the negative control group}) \times 100$$

Data acquisition and analysis were accomplished with FACSDiva 6.2. The strategy for acquiring flow cytometry data, such as region configuration and gating logic, was as described in the 96-well In Vitro MicroFlow Kits manual. The following parameters were calculated and a test compound was deemed positive if all of the following criteria are met:

Parameters:

(i) Frequency of micronuclei relative to main nucleus (%MN/% MicroNuclei)

(ii) Ratio of micronucleus frequency to simultaneous negative controls (fold MN)

(iii) Cytotoxicity indicators include the EMA positive ratio (fold EMA/fold ethidium monoazide) and the RPD (relative population doubling) for concurrent negative controls after 24 h culture.

MDR1 Substrate Screening Assay. Human MDR1-expressing MDCK cells were cultured, and the transcellular transport study was performed. The cells were grown in a transwell 96-well permeable support (pore size 0.4 μm, 0.143 cm^2 surface area) with a polycarbonate membrane (Corning Life Sciences, Lowell, MA). The cells were preincubated with HBSS for 10 min at 37 °C. Subsequently, transcellular transport was initiated by the addition of HBSS either to apical compartments (75 μL) or to basolateral compartments (250 μL) containing 10 μM YH-53. The assay was terminated by separating each assay plate after 1 h. Aliquost (25 μL) from the opposite compartments were mixed with acetonitrile. After centrifugation, the compound concentrations in the supernatant were measured by LC/MS/MS, using a UFLC system coupled to a Triple QUAD 5500 and an Unison UK-C18 HT column (3.0 μm, 2.0 × 20 mm). The apparent permeability of YH-53 in the receiver wells was determined, and the efflux ratio (ER) for the membrane permeability test was calculated using the following equation:

$$\mathrm{ER} = \mathrm{Papp,BtoA}/\mathrm{Papp,AtoB}$$

where Papp,AtoB and Papp,BtoA represent the apparent permeability in the apical-to-basal direction and the basal-to-apical direction, respectively.

***In Vivo* Pharmacokinetic Study of YH-53 in Rats.** An *in vivo* pharmacokinetic study in rats was carried out as described previously.[48,49] Male Wistar rats were housed three per cage with free access to commercial chow and tap water and were maintained on a 12 h dark/light cycle (08:00−20:00 light) in an air-controlled room (temperature, 24.0 ± 1 °C; humidity, 55 ± 5%). All animal experimental protocols were reviewed and approved by the Committee of Animal Care and Welfare of Kanazawa University. Male Wistar rats (230−250 g, body weight) that fasted overnight were anesthetized by isoflurane. The right jugular veins of rats were cannulated with silicone tubing (100−00N; 0.5 mm I.D., 1.0 mm O.D., Kaneka Medical Products). YH-53 was administrated via the left jugular veins (i.v. administration, 0.1 mg/kg) or orally administrated by gavage (p.o. administration, 0.5 mg/kg) with YH-53 in saline. The rats were moving freely and not anesthetized during the experiment. Blood samples (500 μL) were collected from the cannula into heparinized tubes at designated times up to 7 h. Each blood sample was replaced with an equal volume of saline, and heparinized saline was used to maintain the patency of the catheter. Blood samples were centrifuged at 3000 rpm for 10 min. The resultant plasma was stored at −30 °C until analysis. The plasma concentration of YH-53 was measured using a LC-MS/MS system consisting of an AB-Sciex API 5000 triple quadrupole mass spectrometer (AB SCIEX, Foster City, CA) coupled with a LC-20AD ultrafast liquid chromatography (UFLC) system (Shimadzu Company, Kyoto, Japan). An Agilent ZORBAX Eclipse Plus (C18, 50 × 2.1 mm, 5 μm) was used as the analytical column. A mobile phase composed of 0.1% formic acid (A) and acetonitrile (B) was used at a flow rate of 0.4 mL/min with a gradient elution. The mass transitions (Q1/Q3) of *m*/*z* 576.2/290 and 260.2/116.0 were used for YH-53 and propranolol (as an internal standard), respectively. Analyst software version 1.7.2 (AB SCIEX) was used for data analysis. Plasma concentration−time curves of YH-53 were plotted and analyzed. The area under the plasma concentration−time curve from 0 to 7 h (AUC_{0-7}) and from 0 to ∞ ($AUC_{0-\infty}$) was calculated by the trapezoidal method using non-compartmental analysis with the MOMENT program.[50] The maximum plasma concentration (C_{max}) and the time to reach C_{max} (t_{max}) were obtained directly from the experimental data. The elimination half-life ($t_{1/2}$) was calculated based on the terminal elimination rate constant determined by log−linear regression of the final data points (at least 3). Also, the compartment model analysis was calculated using the numerical analysis program Napp.[51]

Transport Experiments of YH-53 Using Caco-2 Cells. An *in vitro* permeability assay using Caco-2 cells was carried out as described previously.[52] The Caco-2 cell line was obtained from American Type Culture Collection (Rockville, MD). Caco-2 cells were cultured at 37 °C in a humidified atmosphere of 5% CO_2 in air using DMEM supplemented with 10% FBS, 1% L-glutamine, 1% NEAA, and 5% antibiotic−antimycotic solution. Cells were routinely subcultured at 90% confluency with trypsin-EDTA. For transport studies, Caco-2 cells were plated onto cell culture inserts (3.0 μm pores, 0.9 cm^2 growth area) at a density of 6.4×10^4 cells/insert. The culture medium (0.8 mL in the inset and 2.0 mL in the well) was replaced with fresh medium at 5 days after initiation of cell culture and every 48 h thereafter. After 21 days in culture, the Caco-2 monolayer was utilized for the transport experiments. The cell monolayers were preincubated in transport medium (TM, Hanks' balanced salt solution with 10 mM HEPES, pH 7.4) for 30 min at 37 °C. After preincubation, transepithelial electrical resistance (TEER) of the monolayers was measured routinely before and after each experiment. Then the study was initiated by adding the test drugs (YH-53, metoprolol, or atenolol) to the donor (apical, AP) side and TM to the receiver (basal, BL) side. Metoprolol and atenolol were used as high- and low-permeability model drugs, respectively. Samples were obtained from the receiver side at 30, 60, 90, and 120 min. All experiments were performed at 37 °C. The amount of YH-53 was measured using a LC-MS/MS system. The permeability (apparent

https://doi.org/10.1021/acs.jmedchem.1c00665
J. Med. Chem. XXXX, XXX, XXX−XXX

permeability coefficient, cm/s) of each drug was calculated according to the following equation:

$$\text{permeability} = 1/A \times C_D(dQ/dt)$$

where Q is the amount of compound transported over time t (therefore, dQ/dt is the amount of compound transported within a given time period [μmol/s]). C_D is the initial concentration of compound in the donor compartment (μM), and A is the membrane surface area (cm^2).

Metabolic Analysis. Cryopreserved human hepatocytes were purchased from Thermo Fisher Scientific (Waltham, MA). Cryopreserved rat hepatocytes were obtained from BioIVT (Westbury, NY). The hepatocytes were suspended with InVitroGRO KHB buffer (BioIVT) to prepare 6×10^5 viable cells/mL. YH-53 (10 μM) was added into the hepatocytes and incubated for 0 and 2 h at 37 °C in a humidified atmosphere containing 5% CO_2. Reactions were terminated by the addition of acetonitrile. After centrifugation, aliquots of the supernatant were injected into a LC/UV/MS system for metabolite analysis. The metabolites formed during the incubation were detected at a UV wavelength of 295 nm. The metabolite structure was presumed based on the protonated or deprotonated molecule and the product ion spectrum data.

■ ASSOCIATED CONTENT

Supporting Information

The Supporting Information is available free of charge at https://pubs.acs.org/doi/10.1021/acs.jmedchem.1c00665.

Kinetics, NMR titration, and structure of $3CL^{pro}$; cytotoxicity and antiviral activity of tested compounds with a MDR-1 inhibitor; computational, in vitro metabolic and in vivo pharmacokinetic data of YH-53 (PDF)

Molecular formula string table (CSV)

■ AUTHOR INFORMATION

Corresponding Author

Yoshio Hayashi − *School of Pharmacy, Department of Medicinal Chemistry, Tokyo University of Pharmacy and Life Sciences, Hachioji, Tokyo 192-0392, Japan;* orcid.org/0000-0002-7010-6914; Phone: (+81)42-676-3279; Email: yhayashi@toyaku.ac.jp

Authors

Sho Konno − *School of Pharmacy, Department of Medicinal Chemistry, Tokyo University of Pharmacy and Life Sciences, Hachioji, Tokyo 192-0392, Japan*

Kiyotaka Kobayashi − *School of Pharmacy, Department of Medicinal Chemistry, Tokyo University of Pharmacy and Life Sciences, Hachioji, Tokyo 192-0392, Japan*

Miki Senda − *Structural Biology Research Center, Institute of Materials Structure Science, High Energy Accelerator Research Organization (KEK), Tsukuba 305-0801, Japan;* orcid.org/0000-0003-3863-4503

Yuta Funai − *Faculty of Pharmacy, Institute of Medical, Pharmaceutical and Health Sciences, Kanazawa University, Kanazawa 920-1192, Japan*

Yuta Seki − *Faculty of Pharmacy, Institute of Medical, Pharmaceutical and Health Sciences, Kanazawa University, Kanazawa 920-1192, Japan*

Ikumi Tamai − *Faculty of Pharmacy, Institute of Medical, Pharmaceutical and Health Sciences, Kanazawa University, Kanazawa 920-1192, Japan;* orcid.org/0000-0003-4388-083X

Laura Schäkel − *Pharmaceutical Institute, Pharmaceutical & Medicinal Chemistry, University of Bonn, Bonn 53121, Germany*

Kyousuke Sakata − *School of Life Sciences, Tokyo University of Pharmacy and Life Sciences, Hachioji, Tokyo 192-0392, Japan*

Thanigaimalai Pillaiyar − *Pharmaceutical Institute, Pharmaceutical/Medicinal Chemistry, University of Tübingen, Tübingen 72076, Germany*

Akihiro Taguchi − *School of Pharmacy, Department of Medicinal Chemistry, Tokyo University of Pharmacy and Life Sciences, Hachioji, Tokyo 192-0392, Japan*

Atsuhiko Taniguchi − *School of Pharmacy, Department of Medicinal Chemistry, Tokyo University of Pharmacy and Life Sciences, Hachioji, Tokyo 192-0392, Japan*

Michael Gütschow − *Pharmaceutical Institute, Pharmaceutical & Medicinal Chemistry, University of Bonn, Bonn 53121, Germany;* orcid.org/0000-0002-9376-7897

Christa E. Müller − *Pharmaceutical Institute, Pharmaceutical & Medicinal Chemistry, University of Bonn, Bonn 53121, Germany;* orcid.org/0000-0002-0013-6624

Koh Takeuchi − *Cellular and Molecular Biotechnology Research Institute, National Institute of Advanced Industrial Science and Technology, Koto, Tokyo 135-0064, Japan;* orcid.org/0000-0002-6227-4627

Mikako Hirohama − *Faculty of Medicine, Transborder Medical Research Center, University of Tsukuba, Tsukuba 305-8575, Japan*

Atsushi Kawaguchi − *Faculty of Medicine, Transborder Medical Research Center, University of Tsukuba, Tsukuba 305-8575, Japan*

Masaki Kojima − *School of Life Sciences, Tokyo University of Pharmacy and Life Sciences, Hachioji, Tokyo 192-0392, Japan*

Toshiya Senda − *Structural Biology Research Center, Institute of Materials Structure Science, High Energy Accelerator Research Organization (KEK), Tsukuba 305-0801, Japan*

Yoshiyuki Shirasaka − *Faculty of Pharmacy, Institute of Medical, Pharmaceutical and Health Sciences, Kanazawa University, Kanazawa 920-1192, Japan*

Wataru Kamitani − *Department of Infectious Diseases and Host Defense, Gunma University Graduate School of Medicine, Maebashi 371-8511, Japan*

Complete contact information is available at: https://pubs.acs.org/10.1021/acs.jmedchem.1c00665

Author Contributions

The manuscript was written through contributions of all authors. All authors have given approval to the final version of the manuscript.

Funding

This work was supported by Japan Agency for Medical Research and Development (AMED) (20fk0108267s0101 to M.K., Y.S., W.K. and Y.H.) This work was partly supported by CREST, Japan Science and Technology Agency (JST) (JP20356709 to T.S., K.T., A.K. and Y.H.) and Grant-in-Aid for Scientific Research (B) (19H03356 to Y.H.) and Grant-in-Aid for Research Activity Start-up (20K22723 to S.K.) from the Japan Society of the Promotion of Science (JSPS), and Basis for Supporting Innovative Drug Discovery and Life Science Research (BINDS) from AMED under Grant Number JP20am0101071 to T.S. (support number 2688).

Notes

The authors declare no competing financial interest.

https://doi.org/10.1021/acs.jmedchem.1c00665
J. Med. Chem. XXXX, XXX, XXX−XXX

PDB codes for SARS-CoV-2 3CL^{pro} with bound YH-53 and SH-5 are 7E18 and 7E19, respectively.

■ ACKNOWLEDGMENTS

We greatly appreciate Dr. Rolf Hilgenfeld (Univ. of Lübeck) who kindly gave us SARS-CoV-2 3CL^{pro}-encoding vector. We are grateful for contributions (enzyme expression and purification, assay establishment, and synthesis of substrate, respectively) by Dominik Thimm, Anke Schiedel, Lan Phuong Vu, Ghazl Al Hamwi, Vigneshwaran Namasivayam, Robin Gedschold, Carina Lemke, Vittoria Lopez, Salahuddin Mirza, Miriam Diett, and Katharina Sylvester, University of Bonn.

■ ABBREVIATIONS USED

AMC, 7-amino-4-methylcoumarin; AUC, area under the curve; 3CL^{pro}, three chymotrypsin-like protease; DMSO, dimethyl sulfoxide; DTT, dithiothreitol; DMEM, Dulbecco's modified Eagle's medium; EDTA, ethylenediaminetetraacetic acid; FBS, fetal bovine serum; FDA, U.S. Food and Drug Administration; HBSS, Hank's balanced salt solution; HPLC, high performance liquid chromatography; hERG, human ether-a-go-go related gene; HEPES, 4-(2-hydroxyethyl)-1-piperazineethanesulfonic acid; MDR, multidrug resistance; MTT, 3-(4,5-dimethylthiazol-2-yl)-2,5-diphenyltetrazolium bromide; NADPH, nicotinamide adenine dinucleotide phosphate; NTA, nitrilotriacetic acid; NEAA, nonessential amino acids; PK, pharmacokinetics; PBS, phosphate-buffered saline; PEG, polyethylene glycol; KF, potassium fluoride; RNase, ribonuclease; RMSD, root-mean-square deviation; SEM, standard error of the mean; TCID, tissue culture infectious dose; TMPRSS2, transmembrane protease, serine 2

■ REFERENCES

(1) Zhu, N.; Zhang, D.; Wang, W.; Li, X.; Yang, B.; Song, J.; Zhao, X.; Huang, B.; Shi, W.; Lu, R.; Niu, P.; Zhan, F.; Ma, X.; Wang, D.; Xu, W.; Wu, G.; Gao, G. F.; Tan, W. A Novel Coronavirus from Patients with Pneumonia in China, 2019. *N. Engl. J. Med.* **2020**, *382* (8), 727−733.

(2) Zhou, P.; Yang, X. L.; Wang, X. G.; Hu, B.; Zhang, L.; Zhang, W.; Si, H. R.; Zhu, Y.; Li, B.; Huang, C. L.; Chen, H. D.; Chen, J.; Luo, Y.; Guo, H.; Di Jiang, R.; Liu, M. Q.; Chen, Y.; Shen, X. R.; Wang, X.; Zheng, X. S.; Zhao, K.; Chen, Q. J.; Deng, F.; Liu, L. L.; Yan, B.; Zhan, F. X.; Wang, Y. Y.; Xiao, G. F.; Shi, Z. L. A Pneumonia Outbreak Associated with a New Coronavirus of Probable Bat Origin. *Nature* **2020**, *579* (7798), 270−273.

(3) Li, Q.; Guan, X.; Wu, P.; Wang, X.; Zhou, L.; Tong, Y.; Ren, R.; Leung, K. S. M.; Lau, E. H. Y.; Wong, J. Y.; Xing, X.; Xiang, N.; Wu, Y.; Li, C.; Chen, Q.; Li, D.; Liu, T.; Zhao, J.; Liu, M.; Tu, W.; Chen, C.; Jin, L.; Yang, R.; Wang, Q.; Zhou, S.; Wang, R.; Liu, H.; Luo, Y.; Liu, Y.; Shao, G.; Li, H.; Tao, Z.; Yang, Y.; Deng, Z.; Liu, B.; Ma, Z.; Zhang, Y.; Shi, G.; Lam, T. T. Y.; Wu, J. T.; Gao, G. F.; Cowling, B. J.; Yang, B.; Leung, G. M.; Feng, Z. Early Transmission Dynamics in Wuhan, China, of Novel Coronavirus−Infected Pneumonia. *N. Engl. J. Med.* **2020**, *382* (13), 1199−1207.

(4) Mitsuya, H.; Kokudo, N. Sustaining Containment of COVID-19: Global Sharing for Pandemic Response. *Glob. Heal. Med.* **2020**, *2*, 53−55.

(5) Wu, F.; Zhao, S.; Yu, B.; Chen, Y. M.; Wang, W.; Song, Z. G.; Hu, Y.; Tao, Z. W.; Tian, J. H.; Pei, Y. Y.; Yuan, M. L.; Zhang, Y. L.; Dai, F. H.; Liu, Y.; Wang, Q. M.; Zheng, J. J.; Xu, L.; Holmes, E. C.; Zhang, Y. Z. A New Coronavirus Associated with Human Respiratory Disease in China. *Nature* **2020**, *579*, 265−269.

(6) Pillaiyar, T.; Manickam, M.; Namasivayam, V.; Hayashi, Y.; Jung, S. H. An Overview of Severe Acute Respiratory Syndrome-Coronavirus (SARS-CoV) 3CL Protease Inhibitors: Peptidomimetics and Small Molecule Chemotherapy. *J. Med. Chem.* **2016**, *59*, 6595−6628.

(7) Drosten, C.; Günther, S.; Preiser, W.; van der Werf, S.; Brodt, H.-R.; Becker, S.; Rabenau, H.; Panning, M.; Kolesnikova, L.; Fouchier, R. A. M.; Berger, A.; Burguière, A.-M.; Cinatl, J.; Eickmann, M.; Escriou, N.; Grywna, K.; Kramme, S.; Manuguerra, J.-C.; Müller, S.; Rickerts, V.; Stürmer, M.; Vieth, S.; Klenk, H.-D.; Osterhaus, A. D. M. E.; Schmitz, H.; Doerr, H. W. Identification of a Novel Coronavirus in Patients with Severe Acute Respiratory Syndrome. *N. Engl. J. Med.* **2003**, *348*, 1967−1976.

(8) Jeon, S.; Ko, M.; Lee, J.; Choi, I.; Byun, S. Y.; Park, S.; Shum, D.; Kim, S. Identification of Antiviral Drug Candidates against SARS-CoV-2 from FDA-Approved Drugs. *Antimicrob. Agents Chemother.* **2020**, *64*, e00819−20.

(9) Jan, J. T.; Cheng, T. J. R.; Juang, Y. P.; Ma, H. H.; Wu, Y. T.; Yang, W. B.; Cheng, C. W.; Chen, X.; Chou, T. H.; Shie, J. J.; Cheng, W. C.; Chein, R. J.; Mao, S. S.; Liang, P. H.; Ma, C.; Hung, S. C.; Wong, C. H. Identification of Existing Pharmaceuticals and Herbal Medicines as Inhibitors of SARS-CoV-2 Infection. *Proc. Natl. Acad. Sci. U. S. A.* **2021**, *118*, e2021579118.

(10) Pardo, J.; Shukla, A. M.; Chamarthi, G.; Gupte, A. The Journey of Remdesivir: From Ebola to COVID-19. *Drugs Context* **2020**, *9*, 1−9.

(11) U.S. Food & Drug Administration. *FDA approves first treatment for COVID-19*. https://www.fda.gov/news-events/press-announcements/fda-approves-first-treatment-covid-19 (accessed 2021-01-21).

(12) Zhang, L.; Lin, D.; Sun, X.; Curth, U.; Drosten, C.; Sauerhering, L.; Becker, S.; Rox, K.; Hilgenfeld, R. Crystal Structure of SARS-CoV-2 Main Protease Provides a Basis for Design of Improved a-Ketoamide Inhibitors. *Science* **2020**, *368*, 409−412.

(13) Dai, W.; Zhang, B.; Jiang, X. M.; Su, H.; Li, J.; Zhao, Y.; Xie, X.; Jin, Z.; Peng, J.; Liu, F.; Li, C.; Li, Y.; Bai, F.; Wang, H.; Cheng, X.; Cen, X.; Hu, S.; Yang, X.; Wang, J.; Liu, X.; Xiao, G.; Jiang, H.; Rao, Z.; Zhang, L. K.; Xu, Y.; Yang, H.; Liu, H. Structure-Based Design of Antiviral Drug Candidates Targeting the SARS-CoV-2 Main Protease. *Science* **2020**, *368*, 1331−1335.

(14) Pillaiyar, T.; Meenakshisundaram, S.; Manickam, M. Recent Discovery and Development of Inhibitors Targeting Coronaviruses. *Drug Discovery Today* **2020**, *25*, 668−688.

(15) Hilgenfeld, R. From SARS to MERS: Crystallographic Studies on Coronaviral Proteases Enable Antiviral Drug Design. *FEBS J.* **2014**, *281*, 4085−4096.

(16) Muramatsu, T.; Kim, Y. T.; Nishii, W.; Terada, T.; Shirouzu, M.; Yokoyama, S. Autoprocessing Mechanism of Severe Acute Respiratory Syndrome Coronavirus 3C-like Protease (SARS-CoV 3CLpro) from Its Polyproteins. *FEBS J.* **2013**, *280*, 2002−2013.

(17) Li, C.; Qi, Y.; Teng, X.; Yang, Z.; Wei, P.; Zhang, C.; Tan, L.; Zhou, L.; Liu, Y.; Lai, L. Maturation Mechanism of Severe Acute Respiratory Syndrome (SARS) Coronavirus 3C-like Proteinase. *J. Biol. Chem.* **2010**, *285*, 28134−28140.

(18) Lindner, H. A.; Fotouhi-Ardakani, N.; Lytvyn, V.; Lachance, P.; Sulea, T.; Ménard, R. The Papain-Like Protease from the Severe Acute Respiratory Syndrome Coronavirus Is a Deubiquitinating Enzyme. *J. Virol.* **2005**, *79*, 15199−15208.

(19) Barretto, N.; Jukneliene, D.; Ratia, K.; Chen, Z.; Mesecar, A. D.; Baker, S. C. The Papain-Like Protease of Severe Acute Respiratory Syndrome Coronavirus Has Deubiquitinating Activity. *J. Virol.* **2005**, *79*, 15189−15198.

(20) Hegyi, A.; Ziebuhr, J. Conservation of Substrate Specificities among Coronavirus Main Proteases. *J. Gen. Virol.* **2002**, *83*, 595−599.

(21) Pillaiyar, T.; Wendt, L. L.; Manickam, M.; Easwaran, M. The Recent Outbreaks of Human Coronaviruses: A Medicinal Chemistry Perspective. *Med. Res. Rev.* **2021**, *41*, 72−135.

(22) Sydnes, M. O.; Hayashi, Y.; Sharma, V. K.; Hamada, T.; Bacha, U.; Barrila, J.; Freire, E.; Kiso, Y. Synthesis of Glutamic Acid and Glutamine Peptides Possessing a Trifluoromethyl Ketone Group as SARS-CoV 3CL Protease Inhibitors. *Tetrahedron* **2006**, *62*, 8601−8609.

(23) Bacha, U.; Barrila, J.; Gabelli, S. B.; Kiso, Y.; Mario Amzel, L.; Freire, E. Development of Broad-Spectrum Halomethyl Ketone

https://doi.org/10.1021/acs.jmedchem.1c00665
J. Med. Chem. XXXX, XXX, XXX−XXX

Inhibitors against Coronavirus Main Protease 3CLpro. *Chem. Biol. Drug Des.* **2008**, *72*, 34−49.
(24) Regnier, T.; Sarma, D.; Hidaka, K.; Bacha, U.; Freire, E.; Hayashi, Y.; Kiso, Y. New Developments for the Design, Synthesis and Biological Evaluation of Potent SARS-CoV 3CLpro Inhibitors. *Bioorg. Med. Chem. Lett.* **2009**, *19*, 2722−2727.
(25) Konno, S.; Thanigaimalai, P.; Yamamoto, T.; Nakada, K.; Kakiuchi, R.; Takayama, K.; Yamazaki, Y.; Yakushiji, F.; Akaji, K.; Kiso, Y.; Kawasaki, Y.; Chen, S. E.; Freire, E.; Hayashi, Y. Design and Synthesis of New Tripeptide-Type SARS-CoV 3CL Protease Inhibitors Containing an Electrophilic Arylketone Moiety. *Bioorg. Med. Chem.* **2013**, *21*, 412−424.
(26) Thanigaimalai, P.; Konno, S.; Yamamoto, T.; Koiwai, Y.; Taguchi, A.; Takayama, K.; Yakushiji, F.; Akaji, K.; Kiso, Y.; Kawasaki, Y.; Chen, S. E.; Naser-Tavakolian, A.; Schön, A.; Freire, E.; Hayashi, Y. Design, Synthesis, and Biological Evaluation of Novel Dipeptide-Type SARS-CoV 3CL Protease Inhibitors: Structure-Activity Relationship Study. *Eur. J. Med. Chem.* **2013**, *65*, 436−447.
(27) Thanigaimalai, P.; Konno, S.; Yamamoto, T.; Koiwai, Y.; Taguchi, A.; Takayama, K.; Yakushiji, F.; Akaji, K.; Chen, S. E.; Naser-Tavakolian, A.; Schön, A.; Freire, E.; Hayashi, Y. Development of Potent Dipeptide-Type SARS-CoV 3CL Protease Inhibitors with Novel P3 Scaffolds: Design, Synthesis, Biological Evaluation, and Docking Studies. *Eur. J. Med. Chem.* **2013**, *68*, 372−384.
(28) Breidenbach, J.; Lemke, C.; Pillaiyar, T.; Schäkel, L.; Al Hamwi, G.; Diett, M.; Gedschold, R.; Geiger, N.; Lopez, V.; Mirza, S.; Namasivayam, V.; Schiedel, A. C.; Sylvester, K.; Thimm, D.; Vielmuth, C.; Vu, L. P.; Zyulina, M.; Bodem, J.; Gütschow, M.; Müller, C. E. Targeting the Main Protease of SARS-CoV-2: From the Establishment of High Throughput Screening to the Design of Tailored Inhibitors. *Angew. Chem., Int. Ed.* **2021**, *60*, 10423−10429.
(29) Hattori, S.; Higashi-Kuwata, N.; Hayashi, H.; Allu, S. R.; Raghavaiah, J.; Bulut, H.; Das, D.; Anson, B. J.; Lendy, E. K.; Takamatsu, Y.; Takamune, N.; Kishimoto, N.; Murayama, K.; Hasegawa, K.; Li, M.; Davis, D. A.; Kodama, E. N.; Yarchoan, R.; Wlodawer, A.; Misumi, S.; Mesecar, A. D.; Ghosh, A. K.; Mitsuya, H. A Small Molecule Compound with an Indole Moiety Inhibits the Main Protease of SARS-CoV-2 and Blocks Virus Replication. *Nat. Commun.* **2021**, *12*, 668.
(30) Colombo, É.; Désilets, A.; Duchêne, D.; Chagnon, F.; Najmanovich, R.; Leduc, R.; Marsault, É. Design and synthesis of potent, selective inhibitors of matriptase. *ACS Med. Chem. Lett.* **2012**, *3*, 530−534.
(31) Han, Z.; Harris, P. K. W.; Karmakar, P.; Kim, T.; Owusu, B. Y.; Wildman, S. A.; Klampfer, L.; Janetka, J. W. α-Ketobenzothiazole Serine Protease Inhibitors of Aberrant HGF/c-MET and MSP/RON Kinase Pathway Signaling in Cancer. *ChemMedChem* **2016**, *11*, 585−599.
(32) St-Georges, C.; Désilets, A.; Béliveau, F.; Ghinet, M.; Dion, S. P.; Colombo, É.; Boudreault, P.; Najmanovich, R. J.; Leduc, R.; Marsault, É. Modulating the selectivity of matriptase-2 inhibitors with unnatural amino acids. *Eur. J. Med. Chem.* **2017**, *129*, 110−123.
(33) Dragovich, P. S.; Zhou, R.; Webber, S. E.; Prins, T. J.; Kwok, A. K.; Okano, K.; Fuhrman, S. A.; Zalman, L. S.; Maldonado, F. Z.; Brown, E. L.; Meador, L. W., 3rd; Patick, A. K.; Ford, C. E.; Brothers, M. A.; Binford, L. S.; Matthews, D. A.; Ferre, R. A.; Worland, S. T. Structure-based design of ketone-containing, tripeptidyl human rhinovirus 3C protease inhibitors. *Bioorg. Med. Chem. Lett.* **2000**, *10*, 45−48.
(34) Winn, M. D.; Ballard, C. C.; Cowtan, K. D.; Dodson, E. J.; Emsley, P.; Evans, P. R.; Keegan, R. M.; Krissinel, E. B.; Leslie, A. G. W.; McCoy, A.; McNicholas, S. J.; Murshudov, G. N.; Pannu, N. S.; Potterton, E. A.; Powell, H. R.; Read, R. J.; Vagin, A.; Wilson, K. S. Overview of the CCP4 Suite and Current Developments. *Acta Crystallogr., Sect. D: Biol. Crystallogr.* **2011**, *67*, 235−242.
(35) Kutchukian, P. S.; Dropinski, J. F.; Dykstra, K. D.; Li, B.; Dirocco, D. A.; Streckfuss, E. C.; Campeau, L. C.; Cernak, T.; Vachal, P.; Davies, I. W.; Krska, S. W.; Dreher, S. D. Chemistry Informer Libraries: A Chemoinformatics Enabled Approach to Evaluate and Advance Synthetic Methods. *Chem. Sci.* **2016**, *7*, 2604−2613.
(36) Wishart, D. S.; Knox, C.; Guo, A. C.; Shrivastava, S.; Hassanali, M.; Stothard, P.; Chang, Z.; Woolsey, J. DrugBank: A Comprehensive Resource for in Silico Drug Discovery and Exploration. *Nucleic Acids Res.* **2006**, *34*, 668−672.
(37) Boras, B.; Jones, R. M.; Anson, B. J.; Arenson, D.; Aschenbrenner, L.; Bakowski, M. A.; Beutler, N.; Binder, J.; Chen, E.; Eng, H.; Hammond, H.; Hammond, J.; Haupt, R. E.; Hoffman, R.; Kadar, E. P.; Kania, R.; Kimoto, E.; Kirkpatrick, M. G.; Lanyon, L.; Lendy, E. K.; Lillis, J. R.; Logue, J.; Luthra, S. A.; Ma, C.; Mason, S. W.; McGrath, M. E.; Noell, S.; Obach, R. S.; O'Brien, M. N.; O'Connor, R.; Ogilvie, K.; Owen, D.; Pettersson, M.; Reese, M. R.; Rogers, T. F.; Rossulek, M. I.; Sathish, J. G.; Shirai, N.; Steppan, C.; Ticehurst, M.; Updyke, L. W.; Weston, S.; Zhu, Y.; Wang, J.; Chatterjee, A. K.; Mesecar, A. D.; Frieman, M. B.; Anderson, A. S.; Allerton, C. Discovery of a Novel Inhibitor of Coronavirus 3CL Protease for the Potential Treatment of COVID-19. *bioRxiv*, September 30, **2020**. DOI: 10.1101/2020.09.12.293498.
(38) de Vries, M.; Mohamed, A. S.; Prescott, R. A.; Valero-Jimenez, A. M.; Desvignes, L.; O'Connor, R.; Steppan, C.; Devlin, J. C.; Ivanova, E.; Herrera, A.; Schinlever, A.; Loose, P.; Ruggles, K.; Koralov, S. B.; Anderson, A. S.; Binder, J.; Dittmann, M. A Comparative Analysis of SARS-CoV-2 Antivirals Characterizes 3CLpro Inhibitor PF-00835231 as a Potential New Treatment for COVID-19. *J. Virol.* **2021**, *95*, e01819−20.
(39) Davies, B.; Morris, T. Physiological Parameters in Laboratory Animals and Humans. *Pharm. Res.* **1993**, *10*, 1093−1095.
(40) Hoffman, R. L.; Kania, R. S.; Brothers, M. A.; Davies, J. F.; Ferre, R. A.; Gajiwala, K. S.; He, M.; Hogan, R. J.; Kozminski, K.; Li, L. Y.; Lockner, J. W.; Lou, J.; Marra, M. T.; Mitchell, L. J.; Murray, B. W.; Nieman, J. A.; Noell, S.; Planken, S. P.; Rowe, T.; Ryan, K.; Smith, G. J.; Solowiej, J. E.; Steppan, C. M.; Taggart, B. Discovery of Ketone-Based Covalent Inhibitors of Coronavirus 3CL Proteases for the Potential Therapeutic Treatment of COVID-19. *J. Med. Chem.* **2020**, *63*, 12725−12747.
(41) Yung-Chi, C.; Prusoff, W. H. Relationship between the Inhibition Constant (KI) and the Concentration of Inhibitor Which Causes 50 per Cent Inhibition (I50) of an Enzymatic Reaction. *Biochem. Pharmacol.* **1973**, *22*, 3099−3108.
(42) Kato, R.; Hiraki, M.; Yamada, Y.; Tanabe, M.; Senda, T. A Fully Automated Crystallization Apparatus for Small Protein Quantities. *Acta Crystallogr., Sect. F: Struct. Biol. Commun.* **2021**, *77*, 29−36.
(43) Kabsch, W. XDS. *Acta Crystallogr., Sect. D: Biol. Crystallogr.* **2010**, *66*, 125−132.
(44) McCoy, A. J.; Grosse-Kunstleve, R. W.; Adams, P. D.; Winn, M. D.; Storoni, L. C.; Read, R. J. Phaser Crystallographic Software. *J. Appl. Crystallogr.* **2007**, *40*, 658−674.
(45) Afonine, P. V.; Grosse-Kunstleve, R. W.; Echols, N.; Headd, J. J.; Moriarty, N. W.; Mustyakimov, M.; Terwilliger, T. C.; Urzhumtsev, A.; Zwart, P. H.; Adams, P. D. Towards Automated Crystallographic Structure Refinement with Phenix.Refine. *Acta Crystallogr., Sect. D: Biol. Crystallogr.* **2012**, *68*, 352−367.
(46) Emsley, P.; Cowtan, K. Coot: Model-Building Tools for Molecular Graphics. *Acta Crystallogr., Sect. D: Biol. Crystallogr.* **2004**, *60*, 2126−2132.
(47) Hanwell, M. D.; Curtis, D. E.; Lonie, D. C.; Vandermeersch, T.; Zurek, E.; Hutchison, G. R. Avogadro: An Advanced Semantic Chemical Editor, Visualization, and Analysis Platform. *J. Cheminform.* **2012**, *4*, 17.
(48) Shirasaka, Y.; Suzuki, K.; Nakanishi, T.; Tamai, I. Differential Effect of Grapefruit Juice on Intestinal Absorption of Statins Due to Inhibition of Organic Anion Transporting Polypeptide and/or P-Glycoprotein. *J. Pharm. Sci.* **2011**, *100*, 3843−3853.
(49) Funai, Y.; Shirasaka, Y.; Ishihara, M.; Takemura, M.; Ichijo, K.; Kishimoto, H.; Inoue, K. Effect of Osmolality on the Pharmacokinetic Interaction between Apple Juice and Atenolol in Rats. *Drug Metab. Dispos.* **2019**, *47*, 386−391.
(50) Yamaoka, K.; Nakagawa, T.; Uno, T. Statistical Moments in Pharmacokinetics. *J. Pharmacokinet. Biopharm.* **1978**, *6*, 547−558.

https://doi.org/10.1021/acs.jmedchem.1c00665
J. Med. Chem. XXXX, XXX, XXX−XXX

(51) Hisaka, A.; Sugiyama, Y. Analysis of Nonlinear and Nonsteady State Hepatic Extraction with the Dispersion Model Using the Finite Difference Method. *J. Pharmacokinet. Pharmacodyn.* **1998**, *26*, 495−519.
(52) Shirasaka, Y.; Sakane, T.; Yamashita, S. Effect of P-Glycoprotein Expression Levels on the Concentration-Dependent Permeability of Drugs to the Cell Membrane. *J. Pharm. Sci.* **2008**, *97*, 553−565.

https://doi.org/10.1021/acs.jmedchem.1c00665
J. Med. Chem. XXXX, XXX, XXX−XXX